A Deep Neural Network Based on Prior-Driven and Structural Preserving for SAR Image Despeckling

Cong Lin, Chenghao Qiu, Haoyu Jiang, and Lilan Zou

***Abstract*—Remarkable effectiveness has been demonstrated by deep neural networks in the despeckling task for synthetic aperture radar (SAR) images. However, blurring and loss of fine details can result from many despeckling models due to upsampling and mean-square-error (MSE) loss. Additionally, existing degradation models and prior information are ignored by existing despeckling models, which directly learn the mapping from degraded to clear images. To address these issues, an optimization algorithm for the SAR despeckling task based on the integral-Newton method is proposed in this article. Then, a prior-driven despeckling network is proposed, which can automatically capture the implicit priors in SAR images to replace traditional manually made priors. Furthermore, to make the network focus more on learning the structural prior information of images, a structure-preserving loss function based on the MSE and the Canny edge detection operator is designed, which improves the detail of the network retention ability and speeds up convergence. Outstanding results on both simulated datasets and real SAR images are achieved by the proposed method, as shown by a large number of experimental results. Moreover, significant advantages of the proposed method both visually and quantitatively are revealed by comparison with classical and state-of-the-art despeckling algorithms.**

***Index Terms*—Deep image prior, speckle filtering, structural loss, synthetic aperture radar (SAR).**

NOMENCLATURE

SAR	Synthetic aperture radar.
MSE	Mean square error.
MAE	Mean absolute error.
VIF	Visual information fidelity.
HQS	Half quadratic splitting.
FE	Feature encoder.
FD	Feature Dencoder.
AM	Attention module.
DS	Down sample.
US	Up sample.
PSNR	Peak-signal-to-noise ratio.
SSIM	Structural similarity.
ENL	Equivalent number of looks.
EPD − ROA	Edge preservation degree based on the ratio of average.
MoR	Mean of ratios.
UM	Image quality ratio.

Manuscript received 2 April 2023; revised 30 May 2023; accepted 29 June 2023. Date of publication 5 July 2023; date of current version 19 July 2023. This work was supported by the National Natural Science Foundation of China under Grant 62272109. *(Corresponding authors: Haoyu Jiang; Lilan Zou.)*

Cong Lin, Haoyu Jiang, and Lilan Zou are with the School of Electronics and Information Engineering, Guangdong Ocean University, Zhanjiang 524088, China (e-mail: lincong07@163.com; john_h_y_walter@163.com; zoulilan2015@163.com).

Chenghao Qiu is with the College of Information and Communication Engineering, Hainan University, Haikou 570228, China (e-mail: qiuchenghao125@sina.com).

Data is available on-line at https://github.com/kldys/PDSNet.

Digital Object Identifier 10.1109/JSTARS.2023.3292325

I. INTRODUCTION

SAR plays a crucial role in a range of Earth observation tasks, including disaster monitoring, environmental monitoring, and ocean monitoring. This is due to its numerous advantages, such as multiband capability, strong penetration ability, and all-weather usage range [1]. However, SAR imaging inevitably results in multiplicative speckle noise and artifacts in SAR images. The occurrence of speckle noise in SAR imaging is attributed to various factors such as the roughness of the target surface and the width of the camera beam, resulting in interference effects in the received signal. On the other hand, artifacts are caused by multiple scattering, terrain variations, ionospheric disturbances, and other factors [2]. The edges of targets in SAR images are degraded by this speckle noise, which hinders the reading of image information and the application of SAR images in subsequent tasks, such as target recognition, image segmentation, and scene classification [3], [4], [5], [6]. Despeckling SAR images can restore the overall structural information of the images and facilitate advanced visual processing tasks in revealing the biological information and intrinsic characteristics of the target categories in SAR images. Thus, the removal of speckle noise and preservation of details of images have been an actively researched topic in fields such as earth science, remote sensing, and medical ultrasound imaging [7], [8], [9].

In the past decades, many SAR despeckling methods have been proposed by researchers. Multiview processing techniques were mainly used in early despeckling methods. However, with the expansion of SAR image applications and increased spatial resolution requirements, multiview processing techniques were unable to meet these requirements. During this time, significant developments have been made in spatial-domain filtering algorithms, and many classical filters, such as Lee filter [10], Kuan filter [11], and Frost filter [12], have been proposed. Well noise-suppressing capability is provided by these filters, but they are easily affected by the filter window size and it is difficult to balance the relationship between image denoising and detail retention. The gradient-domain information was extracted by Maji et al. [13] by calculating the numerical value in the spatial domain and exponential layer decomposition was used

to remove background noise, alleviating the influence of the window size in traditional spatial-domain filtering. Aghababaei et al. [14] improved the nonlocal (NL) model and presented an independent, model-free despeckling framework that filters noisy images based on the similarity of subblocks. Good denoising performance was achieved by these two algorithms under low-level noise, but the denoising performance declined under high-level noise. Therefore, researchers have proposed transform-domain filtering algorithms that extract clear original signals from noisy data through different transforms, such as wavelet transform, projection transform, etc. Structural information in the transform domain is effectively used by these algorithms to remove noise. These algorithms have high performance in both denoising effect and computational complexity and have gradually become the mainstream algorithm for SAR image denoising. Multiplicative noise was transformed into additive noise through homomorphic transform by Zhang et al. [15], and an SAR image despeckling method based on weighted sparse representation was presented. The method achieved good results on both synthetic and real-world SAR images. However, these methods are sensitive to the selection of the transform function, and differences in geometric properties in remote sensing images are not considered.

In recent years, there has been a significant advancement in artificial intelligence and deep learning technology, and it has been widely applied in various fields, including computer vision and image processing. Many researchers have utilized convolutional neural networks (CNNs) as the main approach for SAR image speckle reduction. For instance, Qin et al. [16] combined traditional wavelet domain denoising methods with deep learning, using CNNs to automatically learn image denoising thresholds. This approach has achieved high accuracy in SAR image target recognition and noise enhancement tasks, overcoming the reliance on professional experience for threshold setting in traditional transform domain and spatial domain filtering methods. A method combining the classic nonlocal means approach with neural networks was proposed by Cozzolino et al. [17], where the weights of the target pixels were estimated using the CNN with nonlocal layers. It is important to note that in standard CNN-based workflows, noise-free images are required to train the network. However, due to the coherence of SAR imaging, there are no noise-free signals. An effective solution to this issue is to train the CNN by adding artificial speckle functions onto an optical image or dataset used for image recognition (e.g., an ImageNet dataset), instead of using real SAR images. A simple yet effective deep learning model was proposed by Sebastianelli et al. [18] for the denoising task of simulated speckle noise and real SAR images. Liu et al. [19] added artificial noise to natural image datasets and utilized the CNN to extract features from the noise image in the spatial domain and transform domain and further reduce detail loss by separating detail features from the noise features, achieving a good denoising performance. MRDDANet [20] and ASGDNet [21] added simulated speckle noise to optical remote sensing images for network training, which enabled the network to better recognize noise information in the image. However, in optical remote sensing simulated images, there are significant differences between optical remote sensing images and actual SAR images in terms of the imaging mechanism of the device and the distribution of pixel intensity, which diminishes the robustness and generalization capability of SAR filters. In order to address this issue, the utilization of the MuLoG algorithm and multitemporal SAR images to restore pixel intensities in noisy images was proposed by Dalsasso et al. [22]. Furthermore, it was demonstrated that deep neural networks trained on natural images can achieve the same level of performance as networks trained on real SAR images.

The use of multitemporal SAR images and unsupervised algorithms for SAR denoising research has been explored by scholars to improve the denoising performance of SAR images. The multitemporal SAR image denoising method integrates images from multiple observation periods to find similar images and uses these similar images to eliminate noise. Therefore, the true SAR image can be studied by the denoising algorithm using multitemporal SAR images, and the algorithm is more in line with the inherent information of SAR images in the denoising task. For example, the impact of noise was counteracted by RABASAR [23] using the time-sequence information in multitemporal SAR images, avoiding the impact of noise in a single frame image, and ratio images were used to improve the spatial stationary of an image within a time sequence, resulting in more effective denoising than comparing the original multitime and space stacked images. An SAR deep learning filter based on noise reference was presented by Ma et al. [24], which demonstrated satisfactory generalization capacity on single-time datasets by using complementary images from different times in the same area as training references. However, it is difficult to obtain data from different time sequences of the same target for multitemporal SAR images, and the denoising performance of the algorithm depends heavily on the accuracy of image registration, making the algorithm not flexible to use. The inherent information of the original SAR image is used during training by unsupervised algorithms [25], [26] to learn the denoising model, making them more flexible to use compared to multitemporal denoising algorithms. Sparse representation-based denoising methods and autoencoder-based denoising methods are typical unsupervised denoising algorithms. The former represents SAR images as sparse coefficients to learn the denoising model, while the latter trains a network to learn the denoising model. A new end-to-end self-supervised denoising model was presented in [27], which incorporates perceptual features from prelearned CNNs and recovers spatial details through a mixed loss function, maintaining the robustness of the entire time-series image and reducing the uncertainty in SAR images caused by random noise. However, due to the presence of contaminated information in the SAR images used for training in the network, it becomes challenging for the network to accurately extract texture details from the images. This issue may impact the loss of details and image blurring in the restored images. Recently, a self-supervised Bayesian despeckling method was proposed in [28]. This method assumes spatial independence of noise and can effectively preserve the statistical properties and edge information of the images without relying on clear images

for training. This offers a new perspective for self-supervised denoising methods.

In fact, multitemporal sequence denoising methods and self-supervised denoising algorithms are in some cases more difficult to extract texture details correctly from SAR images due to the existence of pollution information like speckle noise and artifacts. Relatively speaking training with simulated images can help the network learn a wider range of detailed information from different scenes, making it more useful for preserving texture information in real SAR image restoration tasks. It should be noted that in most deep learning-based SAR image denoising algorithms, prior knowledge such as observation feature modeling and degradation mechanisms in traditional methods are neglected and the network only learns a direct mapping from low-quality images to high-quality images. Knowledge was transferred and Gaussian prior knowledge and structural boundary prior knowledge were incorporated to improve the VGG-16 network by a scholar [29]. Although great results were achieved in removing speckle noise, multiple iterations were still required, making the algorithm computationally inefficient. A denoising prior-driven deep neural network (DPDNN) for image restoration was presented by Dong based on the finding that convolutional generative networks can capture a large amount of statistical information without learning [30], [31]. The DPDNN improves the generalization ability of the network by learning image prior knowledge, resulting in significant improvements in tasks such as Gaussian denoising, deblurring, and superresolution, but it does not apply to SAR image despeckling tasks.

This article proposes a prior-driven and structural-preserving SAR despeckling framework to tackle the shortcomings of current CNN-based denoising methods and the poor generalization ability of networks trained on simulated SAR datasets, inspired by [30] and [31]. The proposed framework consists of three steps. First, an optimization algorithm that is suitable for the SAR image despeckling task is derived, thus formulating the despeckling task as an optimization problem. Second, a prior-driven despeckling neural network (PDSNet) is introduced to solve the optimization problem, resulting in the best image restoration outcomes. Finally, in order to enable the network to better learn the structural prior information in images, a novel joint loss function is designed for network training. The experimental results demonstrate that the proposed method outperforms state-of-the-art methods in SAR despeckling both visually and quantitatively.

Compared with the previous SAR image despeckling methods, the primary innovations presented in this article can be outlined as follows.

1) An optimization algorithm is derived for the SAR image despeckling task, combining traditional model-based methods with deep learning by utilizing neural networks to learn the noise model, providing better adaptability to nonsimulated noise removal tasks in SAR images.
2) A prior-driven denoising network is proposed. In this network, inherent information is first extracted from the image using a CNN, then passed to the denoiser as prior knowledge for network training. By learning the inherent prior information of various types of images, valuable information for denoising can be extracted by the network, making it adaptable when applied to real SAR images.
3) A joint loss function based on the MSE and the Canny edge detection operator was proposed. The aim of this loss function is to mitigate the blurring of images caused by the upsampling and MSE loss function, and to enhance the ability of the network to preserve image details while accelerating the convergence speed of the network.

The remaining sections of this article will be organized as follows. In Section II, the basic concepts of SAR image denoising and relevant literature will be reviewed. A detailed description of the proposed method will be provided in Section III. In Section IV, a comparison of the proposed method with state-of-the-art methods on both simulated dataset and real SAR images will be presented. Section V discusses the complexity evaluation of various algorithm models. Finally, Section VI concludes this article.

II. Related Works

A. SAR Image Speckle Noise Model

Speckle noise in SAR images is a commonly encountered noise, and its effects can be significant in certain applications. To gain a better understanding of the generation mechanism of speckle noise, this section will introduce the relevant concepts and theories of speckle noise modeling.

SAR speckle noise refers to the nonuniform regions of brightness or darkness in an image with a size of several pixels. Speckle noise typically exhibits a random distribution and is primarily caused by limitations in the hardware or software of the radar system, rather than environmental factors. The generation mechanism of speckle noise is highly complex and influenced by various factors. The most significant factors include the inherent noise of the SAR system and its nonlinear characteristics. Additionally, the nonideal characteristics of the antenna, signal transmission losses, and receiver noise also contribute to the generation of speckle noise. Therefore, all SAR images contain noise information, which can have adverse effects on applications such as feature extraction and target detection. Meanwhile, the coherent speckle noise in the image is more difficult to remove than the additive noise in normal images [32].

In order to eliminate noise information in SAR images, the specific formation mechanism and characteristics of speckle noise in SAR images have been extensively studied. Many researchers have attempted to explain and simulate the formation process of speckle noise through models. Typically, it is assumed that the multiplicative noise in SAR images follows a gamma distribution [33], and its model can be represented as such

$$\mathbf{I}(x, y) = \mathbf{u}(x, y) \times \mathbf{N}(x, y). \tag{1}$$

The coordinates of (x, y) are used to denote the central pixel of the cell in the azimuthal and distance direction. The intensity of each image pixel, which is contaminated by coherent speckle noise, is represented by $\mathbf{I}(x, y)$ as the observed image intensity. The observed true image intensity, which is uncontaminated by coherent speckle noise, is denoted by $\mathbf{u}(x, y)$ as the radar echo

of a random ground target. The coherent speckle noise, which is caused by the fading process, is represented by $\mathbf{N}(x, y)$. It is noted that $\mathbf{u}(x, y)$ and $\mathbf{N}(x, y)$ are independent of each other, and $\mathbf{N}(x, y)$ follows a generalized Gamma distribution

$$\rho(\mathbf{N}) = \frac{L^L \mathbf{N}^{L-1} e^{-L\mathbf{N}}}{\Gamma(L)} \tag{2}$$

where $L > 1$, $\mathbf{N} > \mathbf{0}$, and $\Gamma(\cdot)$ denotes the Gamma distribution function, with L being the number of looks in the SAR image

$$L = \frac{\bar{X}}{\text{var}} \tag{3}$$

where $\bar{X}$ and *var* are the mean and variance of SAR image $\mathbf{I}$.

Combining the aforementioned mathematical model, it can be inferred that SAR image denoising corresponds to the removal of coherent speckle noise $\mathbf{N}$ from the noisy image $\mathbf{I}$. Previous studies have demonstrated that denoising algorithms trained on clean-noisy image pairs exhibit outstanding denoising performance [34]. Therefore, in this study, the aforementioned formula will be employed to add simulated noise to optical remote sensing images, generating clean-noisy image pairs for training the network parameters. Additionally, according to (2), the intensity of coherent speckle noise is influenced by the natural constant e and the number of looks L in the SAR image. Hence, by modifying different values of the number of looks L, we can obtain speckle noise of varying degrees to train the network, thereby enhancing its robustness.

In this study, the aforementioned formula will be employed to simulate speckle noise and add it to optical remote sensing images for training the denoising network. In subsequent experiments, the performance of our proposed model will be compared with other algorithms using reference-based metrics. However, many methods that perform well in simulating noise removal using optical data for training SAR despeckling networks exhibit poor performance in real SAR image denoising tasks. Therefore, in this study, various reference-free metrics will be further employed to evaluate the denoising performance of our proposed model on real SAR images, aiming to demonstrate its generalization ability and practical value.

B. Image Restoration Methods

The methods for image restoration can be divided into two categories: one based on learning, and the other based on a model. In the following, the core ideas of two algorithms related to this work will be briefly reviewed.

1) Learning-Based Methods: With the rapid development of computer hardware, especially the widespread use of Graphics processing units (GPUs), and the advancement of deep learning technology, research into denoising algorithms based on learning has been the focus of an increasing number of scholars. A denoiser is trained using a large number of clean-noisy image pairs. Good image denoising performance has been demonstrated, even in the case of unknown noise levels, i.e., blind denoising tasks, by utilizing neural networks [35]. Although neural network-based algorithms for the SAR image denoising have gained popularity, some researches indicate that, the denoising performance of some early neural network-based methods may not outperform traditional algorithms. One typical traditional method is the BM3D, which has demonstrated strong performance in the SAR image denoising. [36], [37]. This issue has been addressed in recent years by developing feedforward denoising neural networks (DnCNNs), which utilize residual networks and batch normalization algorithms to speed up the training process of the neural network and improve image denoising performance [34]. Subsequently, works have been presented to enhance computational efficiency, such as the use of dilated convolutions in IRCNN [38] and the use of downsampled subimages and noise level maps in FFDNet [39].

2) Model-Based Methods: Traditional model-based methods do not require training and rely on inductive biases as prior knowledge. The chosen prior knowledge determines the performance of these methods. These methods are often framed as an optimization problem with an added regularization term, with the objective function as

$$\mathbf{z}^* = \arg\min_{\mathbf{z}} E(\mathbf{z}; \mathbf{I}) + R(\mathbf{z}) \tag{4}$$

where $E(\mathbf{z}; \mathbf{I})$ is a data-related term, such as MSE, that describes the difference between the reconstructed image and the target image; $\mathbf{z}$ is the reconstructed image; and $R(\mathbf{z})$ is a regularization term that constrains the solution space based on prior knowledge.

The data term $E(\mathbf{z}; \mathbf{I})$ is often determined by the task at hand, and the proposed method for $E(\mathbf{z}; \mathbf{I})$ will be discussed in detail later. The regularization term $R(\mathbf{z})$ is often selected based on general priors on the image, and the role of priors is crucial in model-based image restoration algorithms. Different optimization directions are led by different priors. For instance, piecewise constant signals are modeled well by total variation (TV) [40], but it is not effective in restoring more complex edge and image texture information. Wavelet-based processing [41] is more effective in restoring local image structures based on existing transform matrices. A block-based Gaussian mixture model is built by BM3D [37] by exploiting redundant similar blocks in natural images and extracting the nonlocal self-similarity of the image.

Prior knowledge that is manually designed to reconstruct the image is relied upon by traditional model-based denoising methods, while the mapping from degraded images to clear images is learned by the majority of deep-learning-based methods, ignoring the existing degradation model and prior knowledge. It has been pointed out by some scholars that the statistical information of images in these algorithms is captured by the structure of convolutional generative networks, rather than any learning ability [30].

C. Residual Learning

In recent years, neural-network-based methods have been applied to the reconstruction of SAR images, and good results have been achieved by many researchers. However, simulated noisy images are often used to train the networks because the actual noise distribution of SAR images is unknown. As a result, denoising performance is not ideal when tested on real images. Good denoising results are achieved by the SAR-CNN [42],

which transforms SAR images into the logarithmic space, increases the number of CNN layers, and uses a discriminative model to learn how to reduce SAR image speckles. However, two major problems arise as the network depth increases: one is that it can lead to a difficult or even impossible convergence of the network during long-term training; the other is that the network performance will gradually saturate and even start to decline, resulting in the phenomenon of deep network degradation.

The issue of declining performance of network models, specifically the reduction in training accuracy as the network depth increases, was initially addressed by residual learning in CNNs [43]. The residual learning approach assumes the existence of an optimally layered network and implements redundant layers to perform identity mapping, ensuring that the input and output are completely identical after passing through the identity layer. With such a residual learning strategy, extremely deep CNNs can be easily trained, and better accuracy has been achieved in image classification and object detection tasks.

III. Proposed Method

In this section, the problem of speckle reduction in SAR images is addressed by introducing a forward residual network framework based on prior driven. The SAR despeckling model is solved using the variable splitting technique and HQS method, which separates data items and prior information to guide the iteration optimization process based on the prior information of the image. To solve this optimization problem, a prior-driven forward residual despeckling network PDSNet is proposed, with the parameters of the recovered image being the weights of the network to achieve an end-to-end optimization of the denoiser and parameters. Additionally, a corresponding denoiser based on the U-Net network architecture is designed, with the denoiser module divided into feature extraction and image reconstruction parts to quickly and accurately capture noise features. Finally, a structural preservation loss function that combines MSE and the Canny edge detection operator is designed to enhance the ability of the network to preserve image details and accelerate network convergence.

A. SAR Image Speckling Strategy

The optimization problem in (1) and (4) can typically be addressed through the utilization of the variable splitting technique [44], which separates the data term and the regularization term while introducing an auxiliary variable $\mathbf{d}$. As a result, (1) and (4) can be reformulated as

$$(\mathbf{z},\mathbf{d}) = \arg\min_{\mathbf{z},\mathbf{d}} \frac{1}{2}\left\|\mathbf{z}^* - \mathbf{N}\cdot\mathbf{z}\right\|_2^2 + \lambda\Phi(\mathbf{d}),\ \text{s.t. } \mathbf{z}=\mathbf{d} \quad (5)$$

where $\lambda\Phi(\mathbf{d})$ is the weighted term of $R(\mathbf{z})$. The ideal solution of the original equation (4) is the solution that minimizes both the data term and the regularization term weighted by the parameter λ. Based on this, the equality-constrained optimization problem can be transformed into an unconstrained optimization problem using the semiquadratic splitting method [45]

$$\mathbf{z}_{k+1} = \arg\min_{\mathbf{z}} \frac{\left\|\mathbf{z}^* - \mathbf{N}\cdot\mathbf{z}\right\|_2^2}{2} + \frac{\boldsymbol{\mu}\left\|(\mathbf{z}-\mathbf{d}_k)\right\|_2^2}{2} \quad (6)$$

$$\mathbf{d}_{k+1} = \arg\min_{\mathbf{d}} \frac{\boldsymbol{\mu}\left\|(\mathbf{d}-\mathbf{z}_{k+1})\right\|_2^2}{2} + \lambda\Phi(\mathbf{d}). \quad (7)$$

The problem of solving $\mathbf{z}_{k+1}$ is a quadratic optimization problem that can be solved using a closed-form solution such as $\mathbf{z}=\mathbf{W}^{-1}\mathbf{b}$, where $\mathbf{W}$ is a matrix related to the correlated noise matrix $\mathbf{N}$. $\boldsymbol{\mu}$ is the penalty factor. In general, as the dimension of the $\mathbf{W}$ matrix is high, it is not feasible to directly calculate its inverse matrix. Hence, a Newton–Raphson iterative algorithm with an integral term is proposed to calculate $\mathbf{z}_{k+1}$. Equations (6) and (7) can then be rewritten as

$$\mathbf{z}_{k+1} = \mathbf{z}_k - \left[\frac{\mathbf{W}}{\mathbf{N^T N}+\boldsymbol{\mu}}\right] \quad (8)$$

$$\mathbf{W} = \mathbf{N^T}\left(\mathbf{N}\cdot\mathbf{z}_k - \mathbf{z}^*\right) + \boldsymbol{\mu}\left(\mathbf{z}_k - \mathbf{d}\right) + \mathbf{H} \quad (9)$$

$$\mathbf{H} = \gamma\sum_{i=0}^{k}\left(\mathbf{z}_{k+1} - \mathbf{z}_k\right) \quad (10)$$

where γ is a positive proportional factor, and $\mathbf{H}$ is the integral term. Since the optimization algorithm proposed in this article is based on a continuous function, it needs to be discretized to meet the computation requirements of computer systems. In the proposed optimization algorithm, the system is controlled using the PID control algorithm to minimize the error. The PID control algorithm is a classical control method widely employed in the field of automatic control. In this approach, the PID algorithm is incorporated into the design of the optimization algorithm to address the optimization problem. Specifically, the derivative of the objective function is used as the input signal, the PID algorithm is employed as the controller, and the corresponding adjustment is output to enable the optimization algorithm to converge faster and more stably toward the optimal solution. The PID algorithm can be modified as

$$\mathbf{z}_{k+1} = K_p\cdot\mathbf{S}_k + \frac{K_pT}{T_i}\sum_{i=0}^{k}\mathbf{S}_i + \frac{K_pT_d}{T}\left(\mathbf{S}_k - \mathbf{S}_{k-1}\right) \quad (11)$$

where $\mathbf{S}_k$ is a steady-state error, K_p, T_i, and T_d represent different system parameters and the integral term is used to eliminate the steady-state error and can adjust the performance of the system in combination with proportional and differential control. Before reaching the node, $\mathbf{S}_i$ is always positive and its integral is always greater than zero. When there is a steady-state error in the system, the error will remain the same value, but the integral will change, meaning that the previous steady-state error value is combined with the proportional control algorithm, and the integral term will continuously work, allowing the output of $\mathbf{x}_k$ to remain increasing and thus eliminating the steady-state error. The subproblem of $\mathbf{d}$ is a neighborhood operator of $\Phi(\mathbf{d})$, and the solution can be obtained through the denoiser: $\mathbf{d}_{k+1} = f(\mathbf{z}_k)$, where $f(\cdot)$ represents the denoiser. In conclusion, the task of despeckling SAR images can be summarized as Algorithm 1.

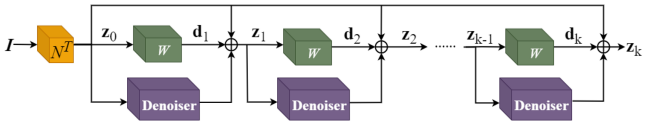

Fig. 1. Core structure of the proposed priori-driven denoising network PDSNet.

Algorithm 1: Restoration of SAR Images by the Integral Newton Iterative Algorithm.

1. Initial the observation matrix $\mathbf{N}$, $\mathbf{W}$, λ, $\mu>0$, $\gamma>0$, $k = 0$, $\mathbf{z}_0 = \mathbf{N^T z^*}$
2. While not converge **do**
  Compute $\mathbf{d}_{k+1} = f(\mathbf{z}_k)$
  Compute $\mathbf{z}_{k+1} = \mathbf{z}_k - \frac{\mathbf{W}}{\mathbf{N^T N}+\boldsymbol{\mu}}$
  $k = k + 1$
 end while
3. Output $\mathbf{z}_{k+1}$

The speckle denoising problem is transformed into an optimization problem using a PID controller, which can preserve image details and edge information while removing speckle noise. Furthermore, the performance of the algorithm can be adaptively adjusted by optimizing the parameters of the PID controller, resulting in improved denoising results in different images.

B. Priori-Driven Residual Networks PDSNet

As indicated in the Related Works section, it is evident that Algorithm 1 for solving the problem necessitates numerous iterations to attain an optimized noise model, which in turn incurs a substantial computational cost. Moreover, the parameters and denoiser cannot be optimized jointly in an end-to-end fashion during the algorithm process. Consequently, our objective is to explore the possibility of capturing the inherent prior images by selecting an appropriate generator network structure before learning any parameters.

Incorporating the ideas from literature [31] and [34], we substitute the denoiser $f(\cdot)$ in $\mathbf{d}_{k+1} = f(\mathbf{z}_k)$ with a neural network in the form $\mathbf{d}_{k+1} = f_\theta(\mathbf{z}_k)$, where θ represents the network parameters, and the network-based $f_\theta(\cdot)$ maps the parameters θ to the denoised signal $\mathbf{d}$. The parameters θ encompass the weights and biases of filters in the network. The network itself has a conventional structure and performs alternating filtering operations, such as linear convolution, upsampling, and nonlinear activation functions. At the same time, the implicit prior is obtained by throwing out the regularizer $R(\mathbf{z})$ and using the neural network to participate in digitization, shown as follows:

$$\theta^* = \arg\min_\theta E\left(f_\theta(\mathbf{d}); \mathbf{z}_0\right), \mathbf{z}^* = f_{\theta^*}(\mathbf{d}). \tag{12}$$

According to the mathematical formulation in (12), Algorithm 1 can be reformulated as the deep CNN architecture shown in Fig. 1, referred to as PDSNet. The proposed network can precisely implement the t iterations in Algorithm 1 to obtain the noise information in the noisy image. The input degraded image $\mathbf{I}$ is first passed through a linear layer parameterized by the degradation matrix $\mathbf{N}$ to obtain the initial estimate $\mathbf{z}_0$. Then, $\mathbf{z}_0$ is fed into the denoising module and a linear layer parameterized by the matrix W, followed by adding a weighted denoising signal $\mathbf{d}_1$ to the output of the linear layers $\mathbf{N}$ and $\mathbf{W}$, resulting in an updated $\mathbf{z}_1$ through the shortcut connection of a residual network. By iteratively repeating this process, the corresponding noise signal $\mathbf{z}_k$ can be obtained.

None of the aspects of this prior network $f_\theta(\cdot)$ are learned in advance by learning from the data, thus it has performance similar to manually set priors like using the TV norm. The contribution of this article is that it demonstrates the effectiveness of the prior-driven network architecture for various image restoration tasks and performs even better than traditional learning methods with manually crafted priors, which will be shown in Section IV.

C. Denoiser Module

For the denoiser module in Fig. 1, we combined the neural network structures presented by U-Net [46] to design a denoiser module. As shown in Fig. 2, the denoiser module is comprised of 13 layers and divided into two distinct parts: a feature encoding part and a feature decoding part.

In the encoding part, a series of convolution layers with a size of 3×3 and a nonlinear ReLU function compose the feature encoder, as shown in Fig. 3(b). In this work, downsampling is performed with a scaling factor of 2 along both axes of the feature map in the downsampling layers, and the scaling factor is set to 0.5. The convolution operation is utilized to extract features, while the downsampling operation reduces the size of the feature maps by half. This part aims to extract the original input image features, and simultaneously, decrease the size of the feature maps, providing more effective feature information for subsequent processing.

The pooling layer in the U-Net network simply reduces the image size by scaling, which cannot determine which parts of different images need to be preserved. Therefore, an attention mechanism module replaces the pooling layer in the original U-Net network structure in this article. The purpose of this module is to use the information from the current stage to guide the learning of noise information in the previous stage, thus focusing the network on the significant information in the noise image, ignoring unimportant information, and improving the efficiency and accuracy of information processing. The architecture of the attention mechanism module is depicted in Fig. 3(a), which comprises two components: the channel attention module and the spatial attention module. The channel attention module consists of a maximum pooling layer, an average pooling layer, and a series of convolutional layers, whereas the spatial attention module comprises a convolutional layer and an activation function.

The decoder component, as shown in Fig. 3(c), The purpose of this part is to restore the downscaled feature maps to their original size and merge the feature information from the encoder layers with that from the decoder layers. This allows the network

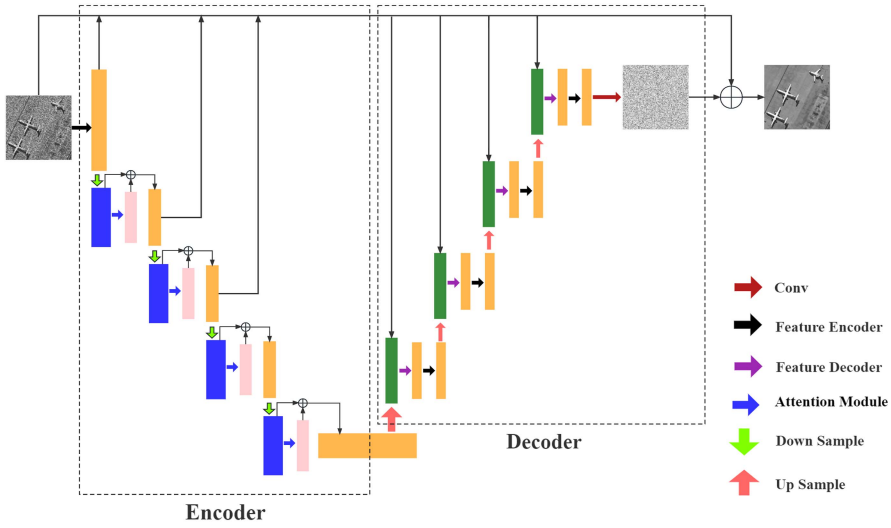

Fig. 2. Framework of denoiser module.

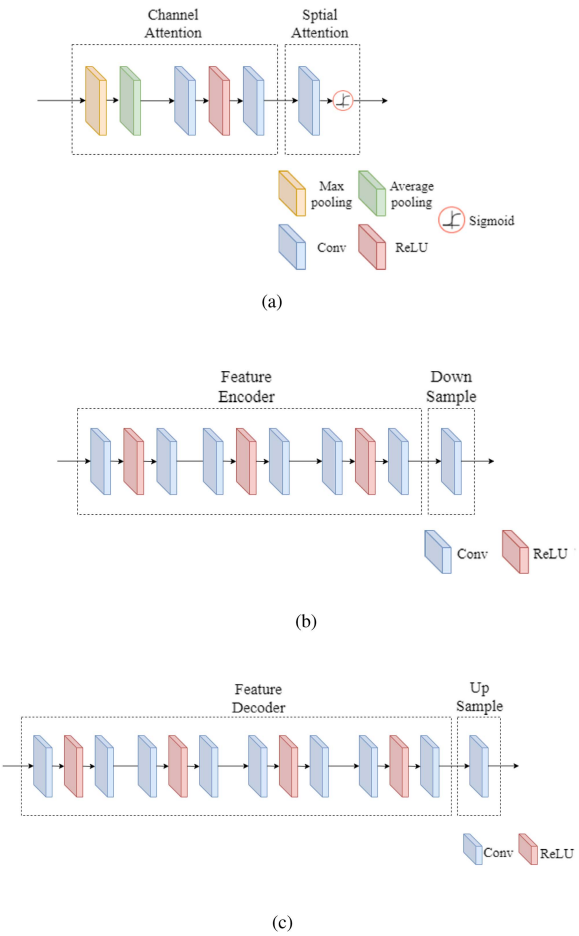

Fig. 3. Specific structure of different modules. (a) Attention module. (b) Feature encoder. (c) Feature decoder.

to have an enhanced generalization capability. It comprises a series of convolutional layers, which are grouped into four feature decoders, as indicated by the purple arrows in Fig. 2. An upsampling layer is utilized subsequently. Given that the final extracted features tend to lose a considerable amount of spatial information, directly using these features to reconstruct the image may result in a lack of detail. To compensate for this limitation, the upsampled feature maps generated in the decoding phase are fused with the feature maps of the same spatial resolution generated in the encoding phase. This way, the original features are preserved, and the lost spatial information is supplemented, resulting in a more fine-grained reconstructed image.

Finally, the algorithm in Fig. 1 uses six such denoisers to help converge, with all parameters forced to be shared to prevent overfitting. In the final step of Fig. 2, this article introduces skip connections from the input to the reconstructed image in the denoising network. By performing a residual operation between the input image and the predicted noise image by the network, the denoised image is obtained. The residual prediction in this step means that during the training phase, the network learns with the goal of predicting the noise of the SAR image, rather than directly predicting the original image. Through residual operation, the texture features of the SAR image can be preserved while removing the noise. This residual learning approach has been proven to be more robust [34]. Table I provides the denoising model and parameter configuration designed in this article.

D. Structural Loss Function

Previous literature [47] has indicated that the utilization of the MSE as the sole loss function may result in smoothened regions in denoised images and poor visual quality. To enhance the ability of the network to preserve edge information and mitigate the blurring effect introduced by upsampling, a structural loss term was proposed in this study to complement the limitations of MSE in the task of image denoising. The proposed joint loss function cannot only guide the training directions of the network, making the network converge faster, but also ensure that the texture information in the repaired image takes into account the

TABLE I
PARAMETER CONFIGURATION OF THE PROPOSED PDSNET

Type	Configuration
Feature encoder	Size of convolution: 64x64x3, padding: 1, ReLU Size of convolution: 64x64x3, padding: 1, ReLU Size of convolution: 64x64x3, padding: 1, ReLU
Downsample	Size of convolution: 64x64x3, padding: 1, stride: 2, ReLU
Attention module	Pooling layer: average pooling layer and maximum pooling layer are parallel Shared MLP: full connection layer1 (64x4x1), ReLU, full connection layer2 (4x64x1), Sigmoid
Upsample	Size of deconvolution: 64x64x3, padding: 1,stride: 2, output_padding: 1
Feature decoder	Size of convolution: 128x3x3, ReLU Size of convolution: 64x64x3, padding: 1, ReLU Size of convolution: 64x64x3, padding: 1, ReLU Size of convolution: 64x64x3, padding: 1, ReLU Size of convolution: 64x64x3, padding: 1
Conv	Size of convolution: 64x1x3, padding: 1

quality and visual effect of the generated denoised image. Given a training set with K pairs of images $\{\mathbf{x}_{\text{noise}}, \mathbf{y}_{\text{ground}}\}_{i=1}^{K}$, the improved loss function is represented as

$$\text{loss}(\Theta) = \frac{1}{2K}\sum_{i=1}^{K}\|\Psi(\mathbf{x}_{\text{noise}};\Theta) - \mathbf{y}_{\text{ground}}\|^2 + \frac{1}{2K}\sum_{i=1}^{K}\|C(\mathbf{x}_{\text{noise}},\alpha_1,\alpha_2) - C(\mathbf{y}_{\text{ground}},\alpha_1,\alpha_2)\|. \tag{13}$$

The first half of (13) represents the traditional similarity loss function based on MSE, and the latter half is the structural loss function added. K represents the number of image pairs without noise, Θ represents the network parameters, $\mathbf{x}_{\text{noise}}$ represents the noisy image input to the network, $\mathbf{y}_{\text{ground}}$ represents the ground truth, $\Psi(\mathbf{x}_{\text{noise}};\Theta)$ represents the reconstructed image obtained through the PDSNet network, and $C(\cdot)$ represents the structural information of the image. α_1 and α_2 are high and low values in the structure information extraction algorithm. According to the experimental results, it was found that the best determination of edge and nonedge pixels in the proposed algorithm was achieved when α_1 and α_2 were set to 50 and 150, respectively. In this article, the Canny operator [48] was improved and selected as the structural information extraction algorithm. The Canny edge detection algorithm has been widely referenced in practical engineering, but in traditional algorithms, a 2×2 neighborhood first-order finite difference is used to calculate the image gradient. This method is simple to calculate but is sensitive to noise information, and because it does not take into account the deviation in the 45° and 135° directions, it is easy to lose real edge information. For images such as SAR images with rich edge information, the traditional edge detection algorithm is not ideal and can easily lose local feature edge information. Therefore, this article introduces the concept of gravity field intensity to replace the image gradient.

A new edge detection algorithm based on the theory of universal gravitation is presented in reference [49]. It performs better than Sobel and Prewitt operators in single criterion edge extraction and retains more useful edge information while having a good noise suppression. However, due to the calculation of

q[a-1, b+1]	**q**[a, b+1]	**q**[a+1, b+1]
q[a-1, b]	**p**[a, b]	**q**[a+1, b]
q[a-1, b-1]	**q**[a, b-1]	**q**[a+1, b-1]

Fig. 4. 3×3 field pixel point locations.

gravitational intensity by equating the gray level value of each pixel to mass, the performance of the gravitational edge detection algorithm will be greatly different in bright areas (high gray level areas) and dark areas (low gray level areas). When a pixel in a bright area and a pixel in a dark area have the same gradient, the total gravitational force generated in the dark area pixel is smaller than that in the bright area, causing the gradient of some dark area pixels to be insensitive, resulting in loss of edge points. To overcome the difference between the bright and dark regions, the gravitational field strength is introduced. Assuming that $\mathbf{p}$ represents the current observation pixel point and $\mathbf{q}$ is any point in its neighborhood, the gravitational field intensity $\vec{U}(\mathbf{p}, \mathbf{q})$ between them can be calculated by the following formula in this article:

$$\vec{U}(\mathbf{p},\mathbf{q}) = \frac{G\cdot\mathbf{q}(m,n)}{\|\overrightarrow{(m,n)} - \overrightarrow{(a,b)}\|^2}\cdot\frac{\overrightarrow{(m,n)} - \overrightarrow{(a,b)}}{\|\overrightarrow{(m,n)} - \overrightarrow{(a,b)}\|}, \quad \mathbf{q}\in\Omega_{\mathbf{p}}^{s} \tag{14}$$

where $\mathbf{q}(m, n)$ is the gray value of pixel $\mathbf{q}$, G is the gravitational field number, and (a, b) and (m, n) are the coordinate positions of $\mathbf{p}$ and $\mathbf{q}$ pixels in the image, respectively. $\Omega_{\mathbf{p}}^{s}$ represents the collection of other pixel points in the s $\times$ s neighborhood centered on $\mathbf{p}$. This method replaces the original edge gradient algorithm with the gravitational field strength and assumes that the total gravitational field strength produced at each point is a combination of the gravitational field strength produced by the surrounding pixels. The edge point is the point with the highest gradient intensity in the image. Hence, the total field strength of $\mathbf{p}$ can be calculated by the following formula:

$$\vec{U}_{\text{total}} = \sum\vec{U}(\mathbf{p},\mathbf{q}), \mathbf{q}\in\Omega_{\mathbf{p}}^{s}. \tag{15}$$

Assuming $s = 3$, the pixel position in the neighborhood $\Omega_{\mathbf{p}}^{3}$ of pixel $\mathbf{p}$ is shown in Fig. 4. Set the distance between two horizontal or vertical pixels is 1, the distance between two diagonal pixels is $\sqrt{2}$. At the same time, the attraction strength of the observation pixel from the pixels that far away decreases rapidly as the distance increases, so the influence of the gravity strength of the distant pixels can be ignored. Therefore, the horizontal and vertical gravitational strength in neighborhood $\Omega_{\mathbf{p}}^{3}$ can be calculated by (16) and (17), respectively,

$$\vec{U}_h = G\cdot\{\mathbf{q}(a+1,b) - \mathbf{q}(a-1,b) + \frac{\sqrt{2}}{4}\cdot [\mathbf{q}(a+1,b-1) - \mathbf{q}(a-1,b+1) + \mathbf{q}(a+1,b+1) - \mathbf{q}(a-1,b-1)]\}\cdot\vec{\mathbf{i}} \tag{16}$$

$$\vec{U}_v = G \cdot \{\mathbf{q}(a, b+1) - \mathbf{q}(a, b-1) + \frac{\sqrt{2}}{4} \cdot [\mathbf{q}(a-1, b+1) - \mathbf{q}(a+1, b-1) + \mathbf{q}(a+1, b+1) - \mathbf{q}(a-1, b-1)]\} \cdot \vec{\mathbf{j}} \quad (17)$$

where $\vec{\mathbf{i}}$ and $\vec{\mathbf{j}}$ are the unit vectors in the horizontal and vertical directions, respectively, at which point the new gradient size is as

$$\|\vec{U}\| = \sqrt{\vec{U}_h^2 + \vec{U}_v^2}. \quad (18)$$

Letting the constant $G = 1$, the horizontal direction operator $\mathbf{G}_h$ and vertical direction operator $\mathbf{G}_v$ of 3×3 neighborhood can be obtained as

$$\mathbf{G}_h = \begin{pmatrix} -\frac{\sqrt{2}}{4} & 0 & \frac{\sqrt{2}}{4} \\ -1 & 0 & 1 \\ -\frac{\sqrt{2}}{4} & 0 & \frac{\sqrt{2}}{4} \end{pmatrix} \quad (19)$$

$$\mathbf{G}_v = \begin{pmatrix} \frac{\sqrt{2}}{4} & 0 & \frac{\sqrt{2}}{4} \\ 0 & 0 & 0 \\ -\frac{\sqrt{2}}{4} & -1 & -\frac{\sqrt{2}}{4} \end{pmatrix}. \quad (20)$$

The similarity loss in the texture feature space is introduced by the proposed structural loss function, which allows for the details and texture of the image to be better captured and preserved in the process of image restoration. As a result, a more visually appealing restored image is produced, and the oversmoothing effect caused by the mean squared error loss is reduced. Additionally, the optimization direction for the network is more clearly defined, which leads to faster convergence during network training. Various image-processing tasks, such as image denoising, reconstruction, deblurring, etc., can be highly effectively addressed with this combined loss function.

E. Difference Between the Proposed Method and Traditional CNN-Based Method

Fig. 5 illustrates the distinction between the proposed method and the traditional CNN-based method to more effectively comprehend the novelty of the SAR despeckling framework. High-dimensional features of the image extracted by the network are leveraged by conventional CNN-based SAR despeckling models to restore a clean ground truth and attain relatively high denoising accuracy. However, these methods often involve complex optimization problems during the testing stage, leading to a lengthy denoising process and difficulty in achieving high performance without sacrificing computation efficiency. The SAR despeckling problem is considered as a mathematical optimization problem by the proposed method, which is solved iteratively via CNNs to separate noise from the image, making the denoising network a simple discriminative learning problem that can focus on the existing degradation models and prior information within the image. Additionally, to allow the prior term to better assist the network optimization, the method integrates the denoiser and the prior network and unfolds the iteration process into a feedforward neural network, which optimizes the parameters of the denoiser through end-to-end learning. This not only achieves high-precision and high-computation efficiency through deep learning but also integrates prior knowledge, resulting in an exceptional denoising performance.

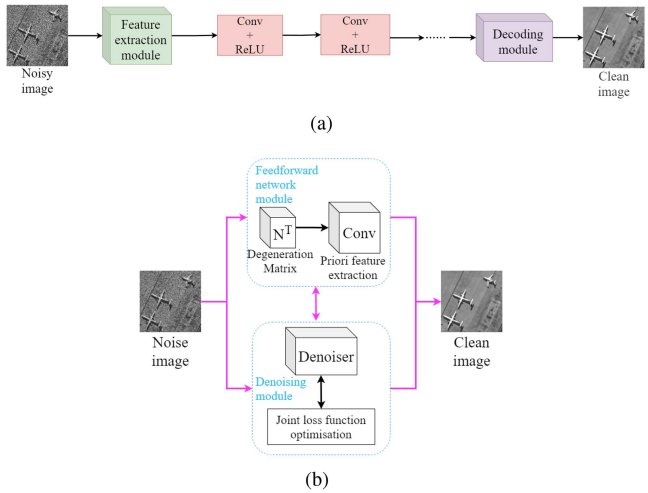

Fig. 5. Overall denoising strategy for the SAR despeckling algorithm. (a) Traditional CNN-based method. (b) Proposed method.

IV. Experimental Results and Discussion

The proposed method trains an SAR despeckling network using optical data, which may lead to a performance degradation when applied to real SAR data. To address this issue, this study incorporates the concept of CNN networks having high impedance characteristics and utilizes the captured real image features by CNN networks as prior information for the subsequent denoising process. To validate the effectiveness of the proposed network, experiments were conducted on both naturally corrupted images with simulated speckle noise and real SAR images. The obtained results demonstrated the superior performance of the proposed method, confirming its efficacy and practicality.

A. Experimental Setup

In the training and testing process, the deep learning network was constructed on the Pytorch 1.11.0 platform. The ADAM optimizer was employed to process minibatches of size 32, with the learning rate initialized at 0.0005 and halved every 45000 minibatch updates. The hyperparameters of ADAM, β_1 and β_2 are set to 0.9 and 0.999, respectively . The operating system used in this study was Ubuntu 20.04, with a GPU of NVIDIA Quadro RTX 6000. The computation ability of the GPU was accelerated through the use of CUDA 11.7 and CUDN 8.6.0, thereby expediting the training process.

To verify the reliability and effectiveness of the algorithm, this article employs the following 11 well-known and advanced learning-based SAR denoising techniques as the benchmark methods.

1) Bayesian shearlet shrinkage for SAR image denoising via sparse representation (BSS-SR) [50].

2) Probability block weighted iterative weighted maximum likelihood SAR image coherent speckle suppression method (PPB) [51].
3) CNN-guided filter for eliminating noise in SAR images (CNN-GFF) [52].
4) Learning deep denoising priors CNN denoising method (IRCNN) [38].
5) Fast and flexible CNN denoising method (FFDNet) [39].
6) CNN and consistent circular rotated SAR image denoising algorithm (CCSNet) [53].
7) Self-supervised denoising algorithm for single noise image (Nb2Nb) [25].
8) Deep self-supervised SAR despeckling algorithm with blind spot CNN (S2V) [28].
9) Self-supervised SAR despeckling method with support from implicit deep denoiser prior (SAR-IDDP) [26].
10) SAR image denoising method based on sharp image features (SIFSDNet) [54].
11) SAR denoising method based on attention and gradient (ASGDNet) [21].

In conducting comparative experiments, the parameters for all the comparison methods were kept identical to those provided in the respective reference literature, thereby ensuring fairness and replicability of the experiments and guaranteeing the reliability of the results. In addition, the code is available for download from the corresponding articles of the authors.

B. Experimental Preparation

1) Training Data: In terms of training data, optical remote sensing images are often used for training despeckling models for SAR images, because they are typically not affected by the multiplicative noise that is commonly encountered in SAR images. This makes it possible to train a despeckling model on optical remote sensing images that can be more effectively applied to SAR images. In addition, optical remote sensing images often have a higher spatial resolution and lower noise levels, which can provide more accurate and reliable reference data, and help to improve the performance and accuracy of the despeckling model. This article selected the NWPU-RESISC45 sensing image public data created by Northwestern Polytechnical University as the training dataset [55]. This dataset comprises 31 500 images, covering 45 scene categories, with 700 images per category, and each image has the same size, and dimensions of 256 × 256. The study randomly selected 800 images as the training set, and after each training phase, ten images not in the training set were selected as the test set.

Due to the fact that the NWPU-RESISC45 dataset consists of color images, which contain more complex and diverse color information and saturation details compared to real SAR images, the task undertaken in this article is primarily focused on enhancing the applicability of the proposed model in SAR image denoising. Therefore, it is necessary to convert the aforementioned NWPU-RESISC45 dataset into grayscale images, allowing the network to better learn the features relevant to SAR image denoising tasks. Additionally, various levels of multiplicative noise were introduced into the training set of simulated data. This facilitates improved learning of textures and fine details similar to those found in SAR images, thereby enhancing the model's capability to handle denoising tasks in real SAR images.

(a) (b) (c)

Fig. 6. Real SAR images. (a) SAR1. (b) SAR2. (c) SAR3.

TABLE II
SAR SATELLITE IMAGING PARAMETERS INVOLVED IN THE THREE IMAGES

Figure	Band	Polarization	Operating mode
SAR1	X	HH, VH, HV, VV	Stripmap, ScanSAR
SAR2	L	HH	Interferometric
SAR3	Ku	HH, HV	Interferometric

2) Test Data: The test data consists of simulated image testing and real SAR image testing. For simulated images, five looks ($L = 1, 2, 4, 8, 10$) were added to four publicly available natural image datasets: classic5 [56], Kodak24 [57], McMaster [58], and Set12 [59]. The pixel intensities of all images in these datasets range from 0 to 255. For each image in these four datasets, the performance of the proposed denoising method as well as other comparative algorithms were tested, and the denoising results were averaged to ensure fair comparison. This testing approach mitigates the possibility of any algorithm excelling on specific images, thus enabling a more accurate assessment of the denoising performance of each algorithm under varying noise conditions.

For the real image test, three real SAR images in different scenarios as shown in Fig. 6 are used to further illustrate the superiority of the proposed algorithm. For convenience, these three images are named SAR1, SAR2, and SAR3, and each has a size of 256 × 256. Fig. 6(a) shows a two-look X-band amplitude image (Bedfordshire) in Southeast England, offering fine spatial resolution and detailed observations of the target area. Fig. 6(b) shows a three-look amplitude image obtained by the airborne system of the Sandia National Laboratories. The airborne system enables SAR data collection from a platform such as an aircraft, allowing for greater flexibility in acquiring images of various areas of interest. Fig. 6(c) shows a four-look Ku-band amplitude SAR image with 1-m resolution over Horse Track, Albuquerque, NM, USA. Compared to X-band, the Ku-band SAR system used for this imagery offers higher frequencies, better penetration of vegetation, and improved target identification.

The aforementioned three images are real SAR images obtained from satellites with the parameters shown in Table II. These three test images represent SAR images obtained through scanning in three different frequency bands, thereby providing a more comprehensive evaluation of the effectiveness of the proposed algorithm in this study.

3) Evaluation Metrics: In the quantitative evaluation of the synthetic dataset, PSNR, SSIM, MSE, MAE, and VIF [60] were used to better demonstrate the superiority of the proposed method. The difference between the restored image and the clean image can be effectively estimated by the PSNR, and the ability of the method for noise suppression is stronger with a higher value, and the restored image is also closer to the clean image. The ability to preserve edges in denoised images can be effectively evaluated by SSIM, and the ability of the algorithm to restore edge details in the image is stronger with a larger value. MSE is measured by calculating the variance of pixel values between two images, while MAE is evaluated by computing the average difference of pixel values between two images. Smaller values of MSE and MAE indicate a closer resemblance between the restored image and the original image. The degree of preservation of image details and structure can be quantified using VIF. A higher VIF value implies a greater capability of the algorithm to preserve image details and structure. Therefore, an increase in the VIF value can indicate an improvement in the algorithm's ability to maintain the image quality.

This article evaluates the performance of various denoising methods using several reference-free indices: ENL [61], EPD-ROA along the horizontal direction (HD) and vertical direction (VD) [62], UM based on first- and second-order descriptors [63], MoR [62], and information entropy. ENL measures the relative strength of speckle noise in an image and the performance of a filter. The higher the ENL value, the smoother the filtered image and the better the filtering effect. EPD-ROA measures the ability of the denoised image to preserve details, the closer its value is to 1, the stronger the ability of the image to preserve details. For ENL and EPD-ROA, if the repaired image is too smooth, the ENL value will be high, because the spatial details and edge preservation are high, making the repaired image lack texture detail information, and the EPD-ROA index is far from 1. Therefore, for SAR image filtering, a filter with excellent performance should be able to ensure that the filtered image is as clean as possible while still retaining a large amount of texture detail information so that it can achieve high performance in both the ENL and EPD-ROA indices. UM measures the overall denoising ability of the image. The smaller the UM value, the better the denoising effect of the algorithm, and the better the overall performance of the denoised image. The closer the MoR value is to 1, the better the preservation of radiation in the repaired image. The magnitude of information entropy represents the amount of information in a denoised image. In general, the denoised image should be simpler than the original image as the impact of noise has been reduced or eliminated, resulting in lower entropy values. Therefore, evaluating the effectiveness of denoising algorithms can be done by calculating the entropy of the denoised image. If a denoising algorithm is successful in reducing the noise and improving the image clarity, the entropy value should decrease.

C. Performance Comparisons on Synthetic Noises

The synthetic data with synthetic speckle noise was used to test the algorithms on two reference metrics, PSNR and SSIM. The test dataset, which contains five levels of speckle noise ($L = 1, 2, 4, 8, 10$), was used to evaluate the performance of different denoising algorithms on four different datasets. The average PSNR and SSIM values obtained by different denoising algorithms on four different datasets are shown in Tables III and IV. The best results are highlighted in bold, and the second-best results are highlighted in red. It is shown that model-based methods, BSS-SR and PPB, are outperformed by PDSNet, indicating that the properties of clean images can be better simulated by deep learning for image restoration tasks compared to traditional manual denoising models. The average PSNR/SSIM values of the proposed network have a significant difference compared to other methods and surpass all comparison techniques. Better denoising ability is demonstrated by PDSNet, which can have a difference in the PSNR of 0.04–4.42 dB and SSIM of 0–0.05 compared to the second-best method. The results of the remaining three metrics, including MSE, MAE, and VIF, are presented in Tables V– VII. Based on the results of these three metrics, it can also be observed that the proposed algorithm exhibits the best performance.

The visual results in Fig. 7 show a comparison between the noise image restoration results of the proposed network and other networks by magnifying some areas. It can be observed from the areas outside the letters in Fig. 7 that PPB, S2V, SIFSDNet, and AGSDNet have better denoising ability and can effectively remove noise in that area. However, the ability of these denoising algorithms to preserve fine details in the image is poor, resulting in blurred letters. Simulated image denoising by several CNN-based methods is also ineffective, and there is still a lot of noise information in the denoised image. Texture information in the image is well preserved by traditional model-based algorithms such as BSS-SR, CNN-GFF, CCSNet, and Nb2Nb based on deep learning, but they cannot completely remove speckle noise. The SAR-IDDP algorithm not only fails to completely eliminate noise information in the image, but also destroys the original texture and detail features in the image. Compared to other methods, the IRCNN shows good denoising performance, but a staircase effect appears in the denoised image, affecting the denoising effect. FFDNet, SIFSDNet, and AGSDNet can effectively suppress noise in the image, but some image details are lost. The proposed denoising model PDSNet has better visual effects compared to the other 11 methods, and the image background can be more accurately identified and denoised, resulting in a result closer to the true image.

D. Performance Comparisons on Real SAR Images

The ability of testing nine denoising algorithms on three real SAR images in Fig. 6 to denoise is further demonstrated. The results of the algorithms on the three images are shown in Figs. 8–10. The performance of the denoising algorithm on the SAR1 image is shown in Fig. 8. The red-bordered areas are marked and magnified for comparison. As can be seen from the figure, speckle noise can be removed to some extent by BSS-SR and S2V, but the denoised image is too blurred, and a lot of texture information is lost. Poor denoising performance is exhibited

TABLE III
AVERAGE PSNR VALUE OF 11 DENOISING METHODS ON FOUR DATASETS

Datasets	L	BSS-SR	PPB	CNN-GFF	IRCNN	FFDNet	CCSNet	Nb2Nb	S2V	SAR-IDDP	SIFSDNet	AGSDNet	Proposed
Classic5	1	26.62	23.54	24.87	26.65	26.56	26.51	25.29	25.33	26.16	25.35	25.19	**26.69**
	2	26.78	24.67	27.33	27.54	27.45	27.42	26.74	26.58	27.03	26.45	26.68	**27.67**
	4	26.86	25.98	27.98	28.46	28.46	28.28	27.11	27.21	27.89	27.85	28.02	**29.40**
	8	26.90	27.01	28.80	29.77	29.53	29.59	28.83	28.19	29.18	29.45	29.45	**30.93**
	10	26.91	27.89	29.12	30.23	30.09	30.20	30.07	29.31	30.12	30.33	30.42	**32.12**
Kodak24	1	25.83	23.86	25.03	26.74	26.82	26.74	25.81	25.05	25.84	25.17	25.68	**27.07**
	2	25.92	25.25	27.47	27.68	27.67	27.57	26.63	25.46	27.08	27.23	27.01	**27.73**
	4	25.97	27.14	28.23	28.85	28.83	28.66	27.48	26.53	28.13	27.99	28.25	**30.13**
	8	25.99	28.00	29.21	30.00	30.29	30.13	29.99	29.23	30.54	29.21	29.36	**31.79**
	10	26.00	28.58	29.62	30.35	30.85	30.71	30.52	29.94	31.28	30.18	30.27	**32.88**
McMaster	1	28.03	25.31	27.08	27.38	27.41	28.22	27.63	26.24	27.85	27.66	27.31	**28.46**
	2	28.17	26.93	28.38	28.56	28.74	28.62	28.12	27.84	28.10	28.43	28.78	**29.12**
	4	28.24	27.45	29.26	29.39	29.75	29.66	28.97	28.48	29.26	29.43	30.14	**31.85**
	8	28.27	28.14	30.33	30.41	30.99	30.90	30.06	29.13	30.67	31.08	31.35	**33.59**
	10	28.28	28.67	30.71	30.75	31.45	31.36	31.11	30.04	31.33	31.65	32.33	**34.41**
Set12	1	25.67	24.44	26.58	27.03	27.01	26.49	25.41	24.56	25.52	25.37	25.11	**28.75**
	2	25.80	25.12	27.42	27.59	27.26	27.12	26.67	26.15	26.90	26.58	26.58	**29.28**
	4	25.85	26.97	28.08	28.49	28.36	28.35	27.32	27.84	28.04	28.01	27.96	**31.97**
	8	25.88	27.76	28.89	29.56	29.58	29.62	29.16	29.05	30.11	29.22	29.19	**33.46**
	10	25.90	28.13	29.91	29.99	30.14	30.17	30.01	29.89	31.45	30.14	30.15	**35.87**

TABLE IV
AVERAGE SSIM VALUE OF 11 DENOISING METHODS ON FOUR DATASETS

Datasets	L	BSS-SR	PPB	CNN-GFF	IRCNN	FFDNet	CCSNet	Nb2Nb	S2V	SAR-IDDP	SIFSDNet	AGSDNet	Proposed
Classic5	1	0.71	0.57	0.72	0.69	0.68	0.70	0.68	0.65	0.71	0.63	0.62	**0.72**
	2	0.72	0.61	0.74	0.72	0.71	0.72	0.70	0.73	0.73	0.70	0.71	**0.75**
	4	0.72	0.69	0.81	0.75	0.75	0.76	0.74	0.73	0.76	0.73	0.75	**0.82**
	8	0.73	0.71	0.85	0.79	0.76	0.84	0.77	0.78	0.83	0.79	0.79	**0.86**
	10	0.72	0.79	0.85	0.81	0.77	0.85	0.82	0.82	0.88	0.83	0.83	**0.91**
Kodak24	1	0.69	0.59	0.70	0.69	0.69	0.71	0.68	0.66	0.68	0.62	0.64	**0.75**
	2	0.70	0.67	0.71	0.70	0.71	0.71	0.72	0.66	0.71	0.71	0.69	**0.77**
	4	0.70	0.73	0.72	0.79	0.78	0.72	0.76	0.73	0.77	0.74	0.77	**0.84**
	8	0.71	0.81	0.75	0.81	0.73	0.75	0.81	0.80	0.85	0.78	0.78	**0.88**
	10	0.71	0.83	0.76	0.83	0.74	0.76	0.83	0.86	0.89	0.82	0.82	**0.90**
McMaster	1	0.79	0.68	0.76	0.68	0.68	0.70	0.72	0.72	0.80	0.72	0.72	**0.82**
	2	0.80	0.71	0.79	0.70	0.69	0.71	0.80	0.75	0.81	0.75	0.75	**0.83**
	4	0.81	0.74	0.82	0.73	0.72	0.77	0.84	0.80	0.84	0.81	0.81	**0.89**
	8	0.81	0.82	0.84	0.77	0.77	0.80	0.86	0.82	0.88	0.84	0.84	**0.92**
	10	0.81	0.83	0.84	0.81	0.80	0.82	0.88	0.88	0.91	0.88	0.88	**0.95**
Set12	1	0.75	0.60	0.71	0.71	0.70	0.68	0.69	0.64	0.72	0.64	0.64	**0.80**
	2	0.76	0.63	0.72	0.72	0.70	0.70	0.75	0.72	0.77	0.69	0.69	**079**
	4	0.77	0.70	0.72	0.77	0.73	0.73	0.81	0.75	0.82	0.74	0.72	**0.87**
	8	0.77	0.75	0.75	0.79	0.76	0.77	0.84	0.82	0.86	0.78	0.77	**0.89**
	10	0.77	0.79	0.80	0.80	0.79	0.82	0.88	0.84	0.91	0.81	0.81	**0.93**

TABLE V
AVERAGE MSE VALUE OF 11 DENOISING METHODS ON FOUR DATASETS

Datasets	L	BSS-SR	PPB	CNN-GFF	IRCNN	FFDNet	CCSNet	Nb2Nb	S2V	SAR-IDDP	SIFSDNet	AGSDNet	Proposed
Classic5	1	141.61	287.79	211.88	140.63	143.68	145.23	192.34	190.58	157.43	189.71	196.83	**139.34**
	2	136.48	221.86	120.25	114.57	116.97	117.78	137.74	142.91	128.84	147.25	139.66	**111.19**
	4	133.99	164.08	103.53	92.70	92.70	96.62	126.49	123.61	105.70	106.67	102.58	**74.65**
	8	132.76	129.44	85.72	68.56	72.46	71.46	85.12	98.64	78.53	73.80	73.80	**52.49**
	10	132.45	105.70	79.63	61.67	63.69	62.09	63.98	76.20	63.25	60.26	59.03	**39.90**
Kodak24	1	169.86	267.35	204.21	137.75	135.23	137.75	170.64	203.27	169.47	197.73	175.82	**127.67**
	2	166.37	194.12	116.43	110.94	111.19	113.78	141.28	184.96	127.37	123.05	129.44	**109.67**
	4	164.47	125.63	97.74	84.74	85.13	88.53	116.17	144.57	100.02	103.30	97.29	**63.11**
	8	163.71	103.06	78.00	65.03	60.82	63.11	65.17	77.64	57.42	78.00	75.35	**43.06**
	10	163.34	90.17	70.97	59.99	53.47	55.22	57.69	65.93	48.43	62.39	61.11	**33.50**
McMaster	1	102.35	191.46	**127.37**	118.87	118.05	97.97	112.22	154.55	106.68	111.45	120.80	**92.70**
	2	99.10	131.85	94.42	90.59	86.91	89.35	100.25	106.19	100.71	93.34	86.12	**78.54**
	4	97.52	116.97	77.1	74.83	68.88	70.32	82.43	92.27	77.10	74.14	62.96	**42.47**
	8	96.85	99.79	60.27	59.17	51.77	52.85	64.13	79.45	55.73	50.71	47.65	**28.45**
	10	96.62	88.32	55.22	54.71	46.57	47.54	50.36	64.43	47.87	44.47	38.03	**23.55**
Set12	1	176.23	233.93	142.92	128.85	129.44	145.91	187.10	227.55	182.42	188.83	200.48	**86.71**
	2	171.03	200.02	117.78	113.26	122.20	126.21	139.98	157.79	132.76	142.92	142.92	**76.75**
	4	169.08	130.64	101.18	92.06	94.86	95.08	120.53	106.93	102.11	102.82	104.01	**41.31**
	8	167.91	108.91	83.96	71.96	71.63	70.97	78.9	81.67	63.40	77.82	78.36	**29.31**
	10	167.14	100.02	66.39	65.17	62.96	62.53	64.88	66.69	46.57	62.96	62.82	**16.83**

TABLE VI
AVERAGE MAE VALUE OF 11 DENOISING METHODS ON FOUR DATASETS

Datasets	L	BSS-SR	PPB	CNN-GFF	IRCNN	FFDNet	CCSNet	Nb2Nb	S2V	SAR-IDDP	SIFSDNet	AGSDNet	Proposed
Classic5	1	0.0465	0.0663	0.0569	0.0463	0.0468	0.0471	0.0542	0.0539	0.0490	0.0538	0.0548	**0.0461**
	2	0.0456	0.0582	0.0428	0.0418	0.0422	0.0424	0.0458	0.0467	0.0443	0.0474	0.0462	**0.0412**
	4	0.0452	0.0500	0.0397	0.0376	0.0376	0.0384	0.0439	0.0434	0.0402	0.0403	0.0396	**0.0338**
	8	0.0450	0.0444	0.0362	0.0323	0.0333	0.0330	0.0360	0.0388	0.0346	0.0336	0.0336	**0.0283**
	10	0.0450	0.0402	0.0349	0.0307	0.0312	0.0308	0.0312	0.0341	0.0311	0.0303	0.0300	**0.0247**
Kodak24	1	0.0261	0.0327	0.0286	0.0235	0.0233	0.0235	0.0261	0.0285	0.0260	0.0281	0.0265	**0.0226**
	2	0.0258	0.0279	0.0216	0.0211	0.0211	0.0213	0.0238	0.0272	0.0226	0.0222	0.0228	**0.0209**
	4	0.0256	0.0224	0.0198	0.0184	0.0185	0.0188	0.0216	0.0240	0.0200	0.0203	0.0197	**0.0159**
	8	0.0256	0.0203	0.0177	0.0161	0.0156	0.0159	0.0161	0.0176	0.0152	0.0177	0.0174	**0.0131**
	10	0.0256	0.0190	0.0168	0.0155	0.0146	0.0149	0.0152	0.0162	0.0139	0.0158	0.0156	**0.0116**
McMaster	1	0.0202	0.0277	0.0226	0.0218	0.0217	0.0198	0.0212	0.0249	0.0207	0.0211	0.0220	**0.0193**
	2	0.0199	0.0230	0.0194	0.0190	0.0186	0.0189	0.0200	0.0206	0.0201	0.0193	0.0186	**0.0177**
	4	0.0198	0.0216	0.0176	0.0173	0.0166	0.0168	0.0182	0.0192	0.0176	0.0172	0.0159	**0.0130**
	8	0.0197	0.0200	0.0155	0.0154	0.0144	0.0145	0.0160	0.0178	0.0149	0.0142	0.0138	**0.0107**
	10	0.0197	0.0188	0.0149	0.0148	0.0136	0.0138	0.0142	0.0161	0.0138	0.0133	0.0123	**0.0097**
Set12	1	0.0519	0.0597	0.0467	0.0443	0.0444	0.0472	0.0534	0.0589	0.0528	0.0537	0.0553	**0.0364**
	2	0.0511	0.0552	0.0424	0.0416	0.0432	0.0439	0.0462	0.0491	0.0450	0.0467	0.0467	**0.0342**
	4	0.0508	0.0446	0.0393	0.0375	0.0380	0.0381	0.0429	0.0404	0.0395	0.0396	0.0398	**0.0251**
	8	0.0506	0.0408	0.0358	0.0331	0.0331	0.0329	0.0347	0.0353	0.0311	0.0345	0.0346	**0.0211**
	10	0.0505	0.0391	0.0318	0.0315	0.0310	0.0309	0.0315	0.0319	0.0267	0.0310	0.0310	**0.0160**

TABLE VII
AVERAGE VIF VALUE OF 11 DENOISING METHODS ON FOUR DATASETS

Datasets	L	BSS-SR	PPB	CNN-GFF	IRCNN	FFDNet	CCSNet	Nb2Nb	S2V	SAR-IDDP	SIFSDNet	AGSDNet	Proposed
Classic5	1	2.85	2.53	2.69	2.85	2.83	2.84	2.72	2.71	2.81	2.70	2.69	**2.86**
	2	2.87	2.64	2.95	2.94	2.93	2.93	2.86	2.85	2.90	2.83	2.86	**2.97**
	4	2.88	2.78	3.02	3.05	3.05	3.03	2.91	2.91	2.99	2.98	3.00	**3.17**
	8	2.88	2.89	3.12	3.20	3.16	3.20	3.09	3.03	3.15	3.16	3.16	**3.36**
	10	2.88	3.01	3.16	3.26	3.22	3.27	3.24	3.16	3.28	3.28	3.29	**3.51**
Kodak24	1	2.77	2.56	2.70	2.85	2.86	2.86	2.76	2.69	2.77	2.68	2.74	**2.91**
	2	2.78	2.71	2.93	2.95	2.95	2.94	2.86	2.72	2.89	2.91	2.88	**2.98**
	4	2.79	2.91	3.01	3.10	3.10	3.05	2.95	2.85	3.02	2.99	3.03	**3.26**
	8	2.79	3.02	3.12	3.23	3.23	3.22	3.23	3.15	3.31	3.14	3.15	**3.46**
	10	2.79	3.09	3.17	3.28	3.29	3.29	3.30	3.25	3.41	3.26	3.27	**3.60**
McMaster	1	3.02	2.72	2.91	2.91	2.91	3.00	2.95	2.82	3.01	2.95	2.92	**3.08**
	2	3.04	2.88	3.05	3.04	3.05	3.05	3.03	2.99	3.03	3.04	3.08	**3.15**
	4	3.05	2.94	3.16	3.13	3.17	3.18	3.14	3.07	3.17	3.17	3.25	**3.47**
	8	3.05	3.04	3.28	3.26	3.32	3.33	3.26	3.14	3.34	3.36	3.39	**3.69**
	10	3.05	3.10	3.32	3.31	3.39	3.39	3.38	3.27	3.42	3.45	3.52	**3.81**
Set12	1	2.78	2.61	2.85	2.89	2.88	2.83	2.73	2.64	2.75	2.71	2.69	**3.10**
	2	2.79	2.68	2.93	2.95	2.91	2.89	2.87	2.81	2.90	2.84	2.84	**3.15**
	4	2.80	2.88	3.00	3.06	3.03	3.03	2.96	2.98	3.03	3.00	2.98	**3.48**
	8	2.80	2.98	3.09	3.18	3.17	3.17	3.16	3.13	3.27	3.14	3.13	**3.66**
	10	2.81	3.03	3.22	3.23	3.24	3.25	3.26	3.23	3.44	3.25	3.25	**3.99**

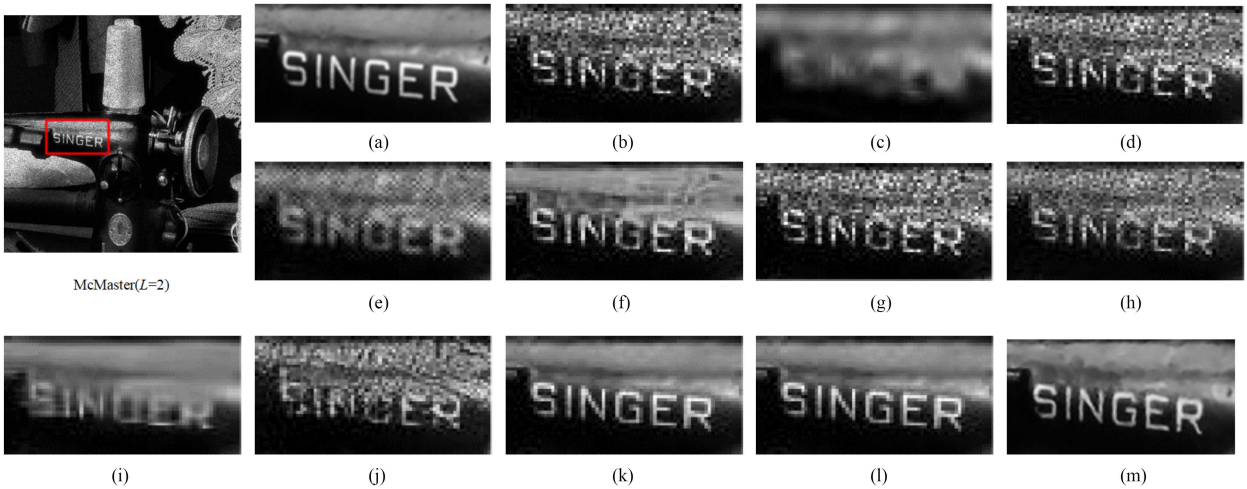

Fig. 7. Denoised results of different methods for image with $L = 2$ speckle noise. (a) Original. (b) BSS-SR. (c) PPB. (d) CNN-GFF. (e) IRCNN. (f) FFDNet. (g) CCSNet. (h) Nb2Nb. (i) S2V. (j) SAR-IDDP. (k) SIFSDNet. (l) AGSDNet. (m) Proposed.

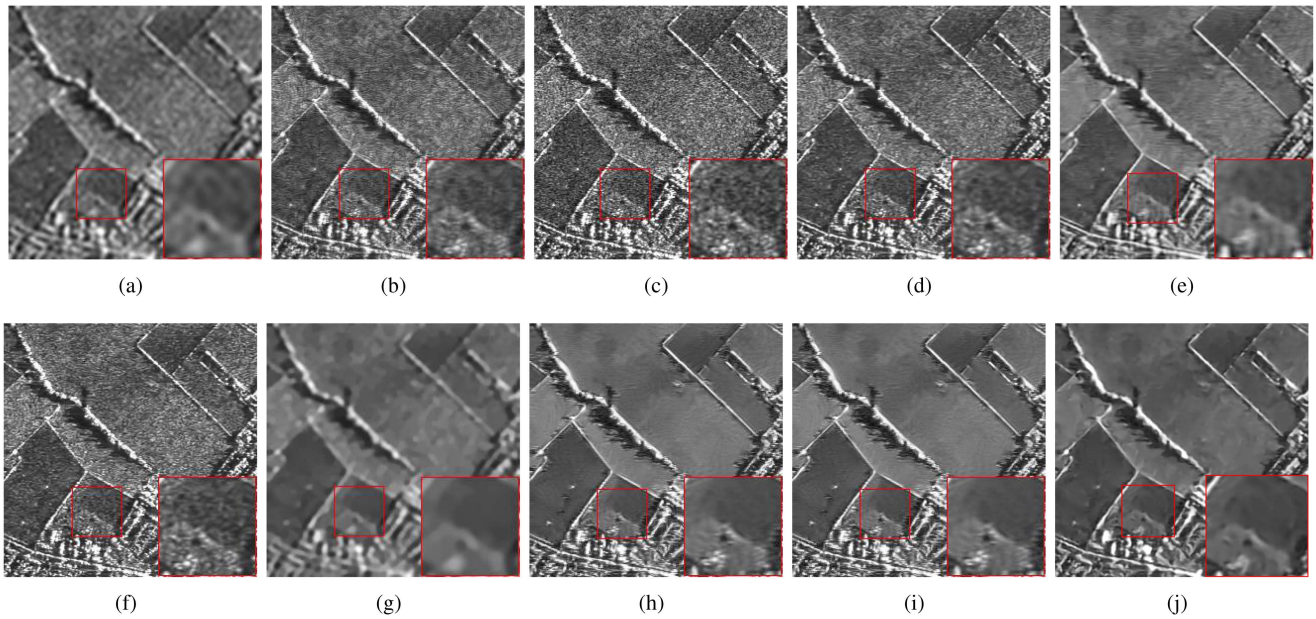

Fig. 8. Performance comparison results of different methods on the real SAR image SAR1. (a) BSS-SR. (b) PPB. (c) CNN-GFF. (d) IRCNN. (e) FFDNet. (f) CCS-Net. (g) S2V. (h) SIFSDNet. (i) AGSDNet. (j) Proposed.

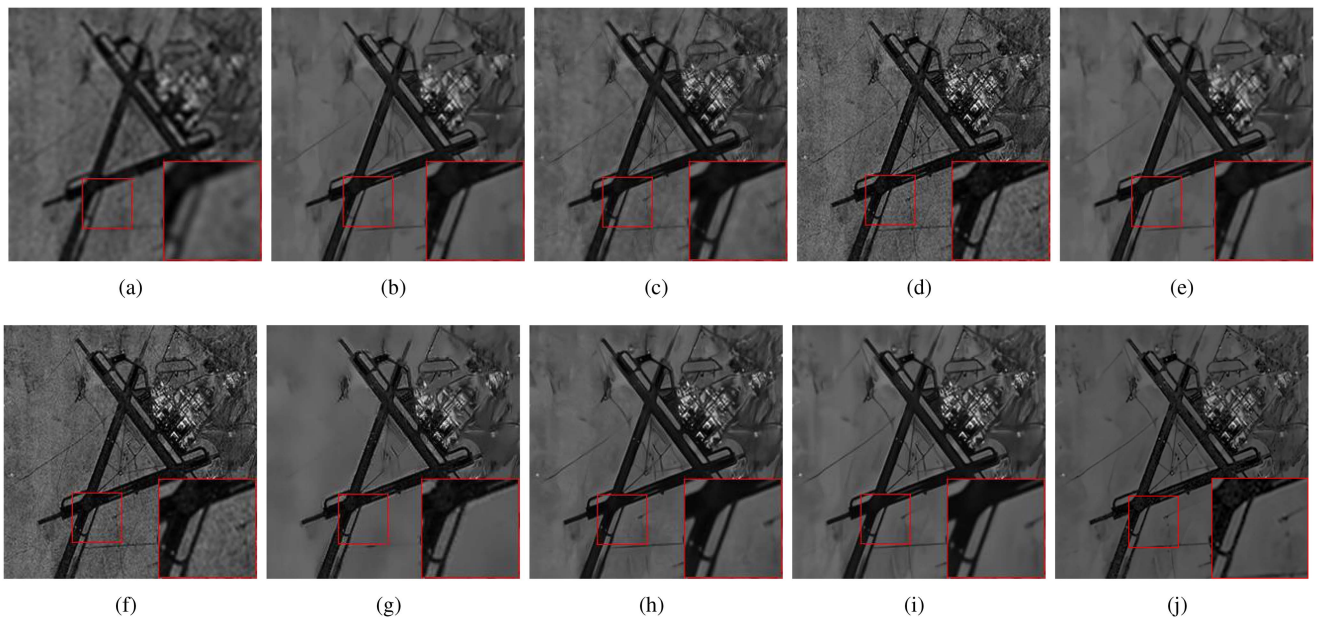

Fig. 9. Performance comparison results of different methods on the real SAR image SAR2. (a) BSS-SR. (b) PPB. (c) CNN-GFF. (d) IRCNN. (e) FFDNet. (f) CCS-Net. (g) S2V. (h) SIFSDNet. (i) AGSDNet. (j) Proposed.

by PPB, CNN-GFF, IRCNN, and CCS-Net. Although they can keep the clear texture information in the image, the noise in the original image has not been removed, and the denoised image is similar to the original noisy image. Good coherence speckle suppression and edge preservation capabilities are demonstrated by FFDNet, SIFSDNet, and AGSDNet algorithms but introduce false shadows in the denoised image. By carefully observing the magnified area, it can be seen that not only does the proposed method PDSNet remove speckle noise better and retain the contours of the blocks in the farmland, but it also does not introduce additional false shadows in the image. Figs. 9 and 10 show the results of the recovery of the other two images. The results are similar to those of SAR1. From the visual effects of Figs. 8–10, it can be seen that, compared to other denoising methods, the details in the image such as the edges can be better preserved by PDSNet, the integrity of the structure of the denoised image can be ensured, and the appearance of blocky effects and false shadows can be suppressed.

Table VIII displays the overall evaluation results of six quality metrics for SAR1 image, with the best results in each column shown in bold and the second-best results in red. From the table, it can be observed that the smallest UM value belongs

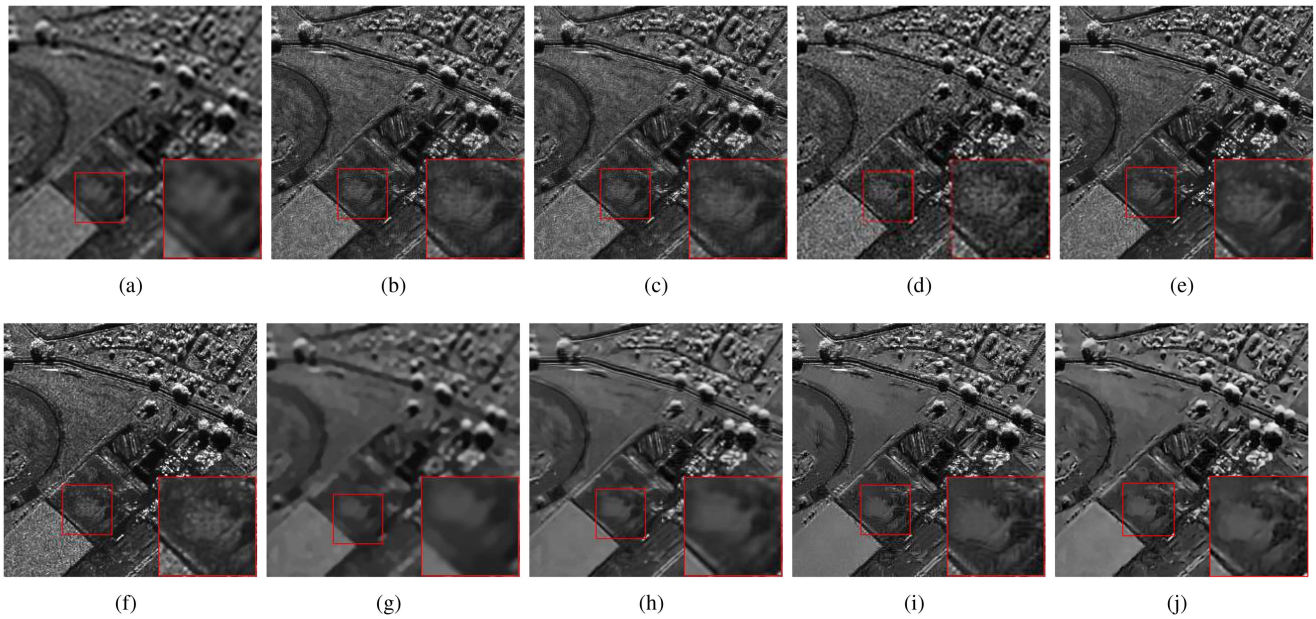

Fig. 10. Performance comparison results of different methods on the real SAR image SAR3. (a) BSS-SR. (b) PPB. (c) CNN-GFF. (d) IRCNN. (e) FFDNet. (f) CCS-Net. (g) S2V. (h) SIFSDNet. (i) AGSDNet. (j) Proposed.

TABLE VIII
OBJECTIVE EVALUATION INDEX VALUES OF DIFFERENT DENOISING METHODS FOR SAR1 IMAGE

Method	ENL	MoR	UM	EPD-ROA-HD	EPD-ROA-VD	Entropy
BSS-SR	4.4079	0.9839	97.0955	0.4763	0.6459	6.97
PPB	4.9700	0.9464	94.9313	0.5744	0.5016	7.18
CNN-GFF	4.0854	0.9759	3420.8	0.7881	0.7835	7.36
IRCNN	4.8984	0.8013	96.1634	0.8031	0.7718	7.17
FFDNet	4.9624	0.9803	222.1988	0.8046	0.7874	7.07
CCSNet	4.8653	0.8959	87.6783	0.9321	0.8976	7.24
S2V	5.3076	0.9852	93.3415	0.8166	0.7924	6.79
SIFSDNet	5.4701	0.9524	338.5627	0.9205	0.9054	7.05
AGSDNet	5.4702	0.9624	345.8649	0.9207	0.8939	6.84
Proposed	**6.0357**	**0.9853**	**82.5173**	**0.9466**	**0.9111**	**6.66**

TABLE IX
OBJECTIVE EVALUATION INDEX VALUES OF DIFFERENT DENOISING METHODS FOR SAR2 IMAGE

Method	ENL	MoR	UM	EPD-ROA-HD	EPD-ROA-VD	Entropy
BSS-SR	6.5498	0.8760	51.5728	0.7050	0.6753	6.50
PPB	7.0206	0.9626	82.1540	0.7296	0.7201	6.40
CNN-GFF	5.8464	0.9772	199.9934	0.7681	0.7455	6.77
IRCNN	6.7507	0.9857	50.9886	0.7316	0.7632	6.55
FFDNet	7.0186	0.9835	50.1246	0.7358	0.7591	6.41
CCSNet	7.1445	**0.9917**	48.9166	0.7751	0.7638	6.46
S2V	7.1264	0.8864	47.7278	0.9386	0.8759	6.35
SIFSDNet	7.2919	0.9509	68.3541	0.9406	0.9248	6.48
AGSDNet	7.2647	0.9868	69.1356	0.9120	0.9204	6.49
Proposed	**7.3020**	0.9884	**35.8438**	**0.9407**	**0.9563**	**5.98**

TABLE X
OBJECTIVE EVALUATION INDEX VALUES OF DIFFERENT DENOISING METHODS FOR SAR3 IMAGE

Method	ENL	MoR	UM	EPD-ROA-HD	EPD-ROA-VD	Entropy
BSS-SR	3.4888	0.8762	69.3165	0.6515	0.5644	6.97
PPB	3.0170	0.9728	81.1955	0.7704	0.6258	7.16
CNN-GFF	2.6489	0.9757	385.9755	0.8395	0.7560	7.16
IRCNN	3.2818	0.9735	69.4630	0.8255	0.7548	7.21
FFDNet	3.3042	0.9644	67.0258	0.8124	0.7569	7.19
CCSNet	3.6082	0.9879	65.8058	0.8408	0.7605	7.23
S2V	3.2507	0.9358	52.7821	0.8495	0.7836	6.83
SIFSDNet	3.9432	0.9717	84.3843	0.8629	0.8225	7.08
AGSDNet	3.7653	0.9788	83.7434	0.8550	0.8121	6.97
Proposed	**3.9720**	**0.9881**	**19.4002**	**0.8644**	**0.8408**	**6.81**

to PDSNet, indicating that PDSNet exhibits the best denoising performance. Additionally, while the highest ENL value also belongs to PDSNet, its EPD-ROA values along HD and VD are also closest to 1, indicating that the best smoothing performance and the best edge preservation ability are provided by PDSNet. In comparison to other methods, PDSNet exhibits a higher MoR value than all other algorithms, indicating that it can achieve better radiation preservation performance. Based on the results obtained from the entropy analysis, it can be observed that the proposed algorithm has also achieved optimal outcomes. This indicates that the algorithm proposed in this article is capable of effectively removing noise from the image and enhancing the clarity of the denoised image. Similarly, Tables IX and X display the repair results of SAR2 and SAR3. From Tables VIII–X, the following can be concluded. First, the smallest UM value belongs to PDSNet, indicating that it has the best overall noise suppression performance. Second, PDSNet exhibits a higher ENL value than all other denoising methods. Third, the EPD-ROA values and MoR along HD and VD are closer to 1, indicating that our method has a better radiation preservation performance and the best edge preservation ability. Finally, the algorithm proposed in this article exhibits superior entropy results compared to any other restoration algorithms.

E. Edge Preservation Performance Comparison

The focus of this study is on the restoration of a large amount of noise present in SAR images using a filtering model, aiming to improve the performance of subsequent tasks such as image segmentation and target recognition. To demonstrate the effectiveness of texture preservation after restoration by various algorithms, images in Figs. 7 and 9 were selected and specific regions were magnified. The Canny edge detection operator was employed to showcase the edge details of the restored SAR images by each algorithm. The visualization results are presented in Figs. 11 and 12.

The Canny edge detection results for the letter region are illustrated in Fig. 11. The aforementioned filtering algorithms, which failed to completely eliminate noise, exhibit a significant presence of false edge information in the edge detection results. Additionally, other algorithms with strong denoising capabilities lead to edge disappearance. In comparison to other algorithms, the edges of the image restored by the proposed algorithm are closest to the edges of the original image.

Upon observing Fig. 12, it can be noted that algorithms (d) and (f) fail to completely remove noise, resulting in the presence of a significant number of false edges in the filtered edge images. On the other hand, algorithms (a), (b), (c), (e), and (g) successfully eliminate noise, but mistakenly remove certain genuine texture information, leading to insufficient richness in texture details. Considering the overall restoration performance of each algorithm, it can be concluded that the proposed algorithm exhibits the best balance, as it achieves the denoising task while better preserving the edge and texture features of the SAR image.

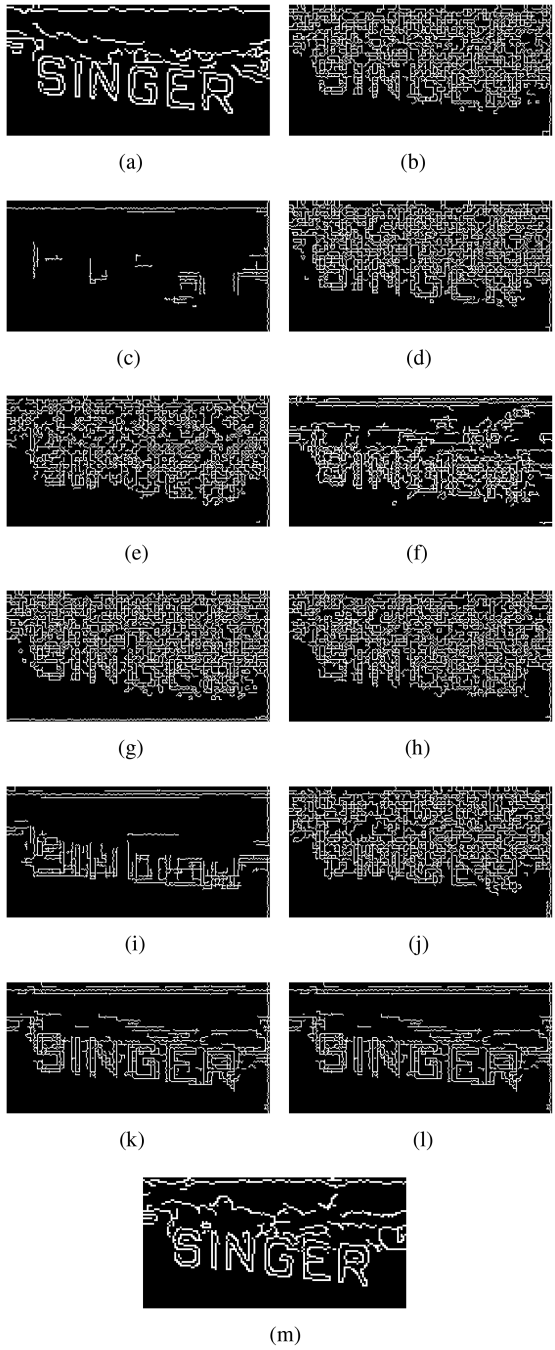

Fig. 11. Edge detection results of simulated speckle noise inpainting. (a) Original. (b) BSS-SR. (c) PPB. (d) CNN-GFF. (e) IRCNN. (f) FFDNet. (g) CCSNet. (h) Nb2Nb. (i) S2V. (j) SAR-IDDP. (k) SIFSDNet. (l) AGSDNet. (m) Proposed.

F. Verifying the Validity of the Improved Loss Function

Figs. 13 and 14, respectively, display the training iteration of PDSNet with the addition of a structured loss and the image restoration effect. As can be seen in Fig. 13, in the initial training stage, using MSE as the loss function has a faster speed, but oscillates and converges slowly in the later stages, requiring 40 rounds of training to complete. In contrast, PDSNet with the added structural loss function demonstrates stability in the training process and converges after 25 rounds. The network with the added structural loss function performs better than the traditional MSE loss function in terms of both training speed and accuracy. This is because the new loss function trains the denoising network in a more determinate direction, effectively accelerating the training speed while ensuring image quality. Additionally, the original image structure is better preserved during the training process, resulting in more significant denoising effects and improved metrics.

A challenge arises in objectively evaluating the effectiveness and visual impact of incorporating a structural loss function due to the lack of a corresponding clean image for SAR images. To address this issue, an airport image with abundant textural details was selected and subjected to speckle noise with a level of $L = 8$. The restoration results are depicted in Fig. 14. The substantial amount of brick pattern information present on the airport's ground in Fig. 14(a) was retained in the lower part of the aircraft after incorporating the structural loss function, as shown in Fig. 14(d). Although the network successfully removed the noise from the image in Fig. 14(b) through the PDSNet network without incorporating a structural loss function, the brick texture features of the airport's ground were lost, as shown in Fig. 14(c). It is important to note that the texture of the brick stripes above the aircraft was not substantial, and following the addition of speckle noise [as shown in Fig. 14(b)], the texture information was almost completely lost. As a result, it is challenging to

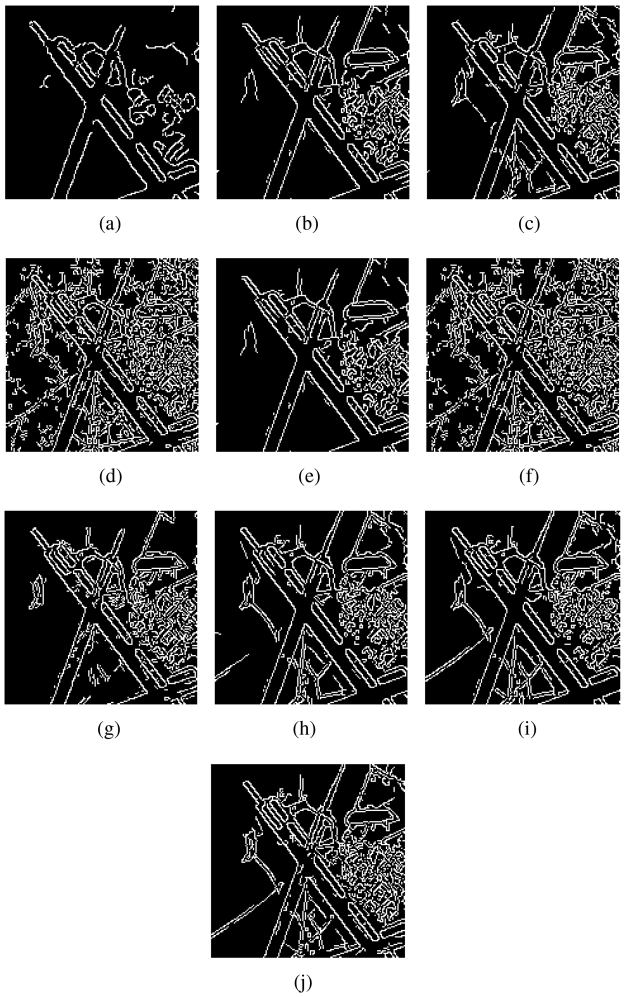

Fig. 12. Edge detection results of real SAR inpainting. (a) BSS-SR. (b) PPB. (c) CNN-GFF. (d) IRCNN. (e) FFDNet. (f) CCSNet. (g) S2V. (h) SIFSDNet. (i) AGSDNet. (j) Proposed.

fully recover the information on these severely damaged brick patterns during the subsequent restoration process.

To further validate the effectiveness and generalization ability of the proposed joint loss function, experiments were conducted on simulated datasets by adding the proposed structural loss function to algorithms that only used MSE as a loss function. Fig. 15 presents a comparison of the results of the algorithm before and after adding the structural loss function in the task of denoising simulated speckle noise in the Set12 dataset for four different L values ($L = 1, 2, 4, 8$). As can be seen from Fig. 15, the addition of the structural loss function significantly improved the performance of the three algorithms in the denoising task. The proposed denoising model PDSNet achieved a maximum improvement of 10% in the SSIM index after adding the structural loss function. The restored image texture was better preserved compared to traditional denoisers that only used mean squared error. Meanwhile, the PSNR index also increased slightly, indicating that the model trained with the joint loss function had better overall denoising performance. In SIFSDNet and AGSDNet, although PSNR decreased by about 2%, the SSIM index increased by up to 14%, indicating that the proposed

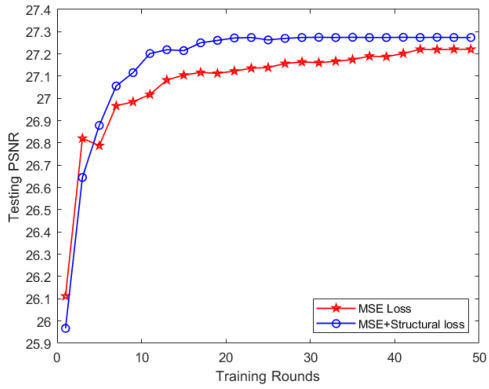

Fig. 13. Testing PSNR performance of PDSNet for different training steps on $L = 1$.

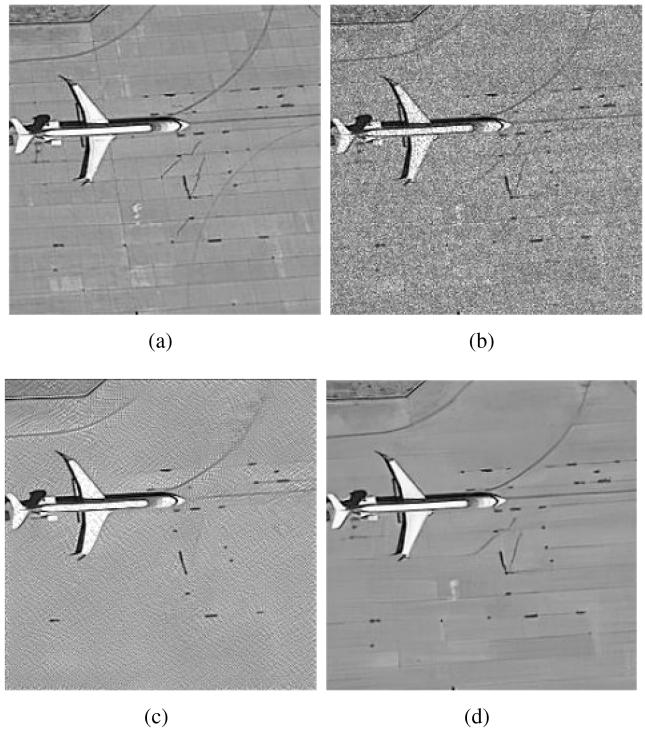

Fig. 14. Improved loss function denoising effect. (a) Original. (b) Noise image. (c) Proposed with MSE loss. (d) Proposed with MSE and structural loss.

joint loss function effectively improved the ability to preserve edge detail information in the task of denoising simulated noise without causing a decrease in the network's performance in denoising speckle noise.

The improved joint loss function was additionally tested on real SAR image denoising, and the results were evaluated using five nonreference metrics, as shown in Table XI. It was observed that the ENL metric, which measures the smoothness of the restored image, decreased for all three algorithms after the addition of the structural loss. However, the UM values also decreased (the smaller the value of UM, the better), indicating an improvement in the combined denoising ability. The EPD-ROA and MoR along HD and VD values got closer to 1, indicating better radiosity preservation and edge preservation

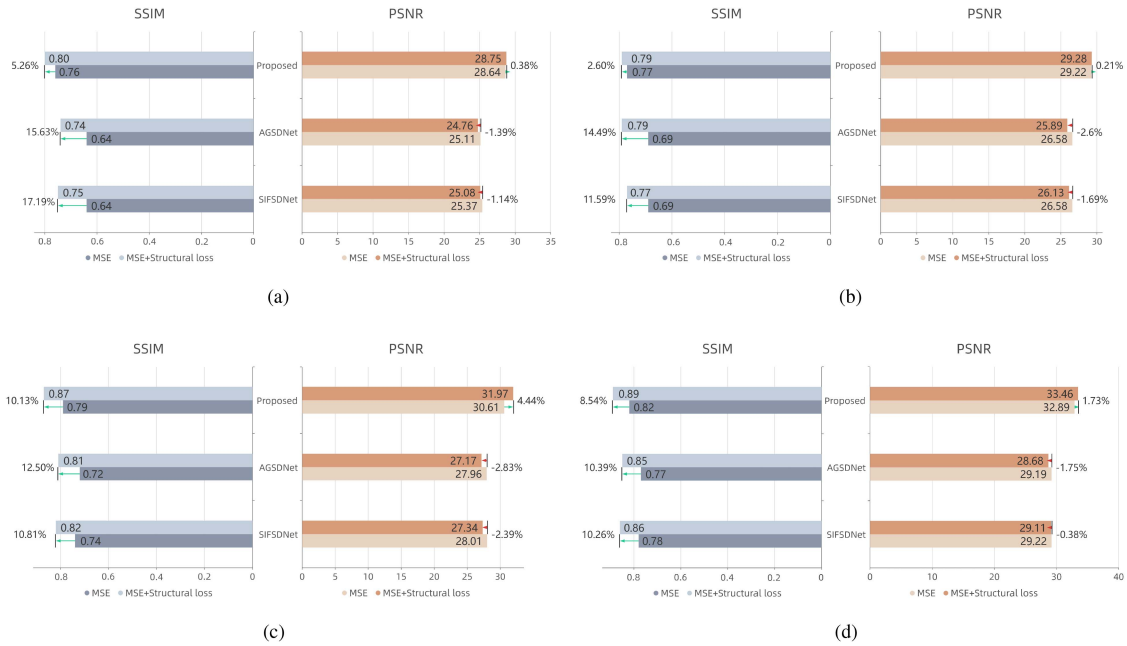

Fig. 15. Synthetic speckle noise restoration results of several speckling methods under different number of views. (a) $L = 1$. (b) $L = 2$. (c) $L = 4$. (d) $L = 8$.

TABLE XI
THE PERFORMANCE OF STRUCTURAL LOSS ON SEVERAL NETWORKS

Method	ENL	MOR	UM	EPD-ROA-HD	EPD-ROA-VD
SIFSDNet+MSE Loss	5.4701	0.9524	338.5627	0.9205	0.9054
SIFSDNet+MSE and Structural Loss	5.3052	0.9612	318.2385	0.9311	0.9273
Change Amplitude	↓ 3.01%	↑ 0.92%	↑ 6.00%	↑ 1.15%	↑ 2.42%
AGSDNet+MSE Loss	5.4702	0.9624	345.8649	0.9207	0.8939
AGSDNet+MSE and Structural Loss	5.3124	0.9669	327.6871	0.9342	0.9075
Change Amplitude	↓ 2.88%	↑ 0.47%	↑ 5.26%	↑ 1.47%	↑ 1.52%
Proposed+MSE Loss	6.8925	0.9514	88.3154	0.9242	0.8962
Proposed+MSE and Structural Loss	6.0357	0.9846	82.5173	0.9466	0.9111
Change Amplitude	↓ 12.43%	↑ 3.49%	↑ 6.57%	↑ 2.42%	↑ 1.66%

performance for the networks trained with the added structural loss function. It is worth noting that the ENL values for the proposed PDSNet algorithm had a significant change after the addition of the structured loss function. This is because PDSNet uses more pooling layers to reduce the size of the image and retain important features, but during the upsampling process, it increases the size of the image without adding the original image information, causing blurring and a higher level of image smoothing. The addition of the structural loss function alleviated the image smoothing problem caused by the MSE loss function and the upsampling process, and ensured the image smoothness while retaining more texture features to achieve better visual effects. The ENI index of PDSNet is not much different from the other two methods after the addition of the structural loss function, which fully proves the effectiveness of the proposed structural loss function.

V. DISCUSSION

This section discusses the complexity evaluation of various algorithm models, including parameter size and testing time. The specific results can be found in Table XII. For algorithms based on traditional filtering methods, only the testing time is provided. And for methods using deep learning, the model parameter sizes and testing times are provided. The testing time is calculated as the average time required to restore three real SAR image data. The experiments for the first two traditional models are conducted using the mentioned CPU, while the experiments for the following six deep learning models are conducted on the mentioned GPU.

The results show that the traditional BSS-SR algorithm is less complex, and thus, faster compared to the PPB algorithm. On the other hand, deep-learning-based algorithms perform better in terms of time. Considering the image restoration results from the previous section, deep-learning-based algorithms outperform traditional methods in terms of performance and restoration speed.

The proposed algorithms have smaller sizes compared to the S2V, SIFSDNet, and AGSDNet models, making them more suitable for deployment and operation on resource-limited embedded devices. By introducing prior knowledge and attention mechanisms, the proposed algorithms can better understand the

TABLE XII
PARAMETER SIZES OF COMPARATIVE MODELS AND AVERAGE TEST TIME

	BSS-SR	PPB	IRCNN	FFDNet	S2V	SIFSDNet	AGSDNet	Proposed
Parameters(MB)	-	-	18.7	**2.59**	15.9	8.25	7.68	5.25
Test time(S)	3.6306	27.5218	2.2789	2.6957	1.2638	**1.2157**	1.8362	2.8641

noise distribution and structural information in SAR images, resulting in more accurate denoising processing. Although this detailed processing approach may increase the computational burden and restoration time, it significantly enhances denoising effectiveness, making the restored SAR images clearer and more usable.

Furthermore, with the continuous improvement of computing power in embedded devices, for resource-limited embedded devices, smaller model sizes mean less storage space and lower memory usage, enabling embedded devices to easily handle SAR image denoising tasks. At the same time, through reasonable optimization and parallelization of algorithms, the restoration time can also be reduced to some extent, making the proposed algorithms more feasible in practical applications.

VI. CONCLUSION

A deep CNN model called PDSNet was proposed, based on prior-driven and structural loss functions, to solve the problem of lack of discriminative ability and loss of details in remote sensing image de-noising. Prior knowledge of remote sensing images and structural loss functions are used by the model to more accurately identify important information, thus accurately removing noise while preserving more texture and detail information. Additionally, an integral term was added to the denoising network to robustly protect against a large amount of noise interference. Experiments were conducted on optical remote sensing images and real SAR images to validate the effectiveness of the proposed algorithm. Comparisons with other denoising methods show that the proposed method has the best visual effect and highest objective evaluation index in terms of suppression of speckle noise and real SAR image noise. Further, results of loss function modification experiments show that the problem of oversmoothing images caused by traditional mean-squared-error-based loss functions can be effectively solved by adding structural loss functions.

The denoised SAR images after the proposed method make an important contribution to improving the accuracy of downstream task image detection and classification. The application of iterative algorithms and related neural networks in various images, including image denoising, deblurring, and superresolution, will be the focus of future research.

REFERENCES

[1] A. Moreira, P. Prats-Iraola, M. Younis, G. Krieger, I. Hajnsek, and K. P. Papathanassiou, "A tutorial on synthetic aperture radar," *IEEE Geosci. Remote Sens. Mag.*, vol. 1, no. 1, pp. 6–43, Mar. 2013.

[2] J.-S. Lee, "Speckle suppression and analysis for synthetic aperture radar images," *Opt. Eng.*, vol. 25, no. 5, pp. 636–643, 1986.

[3] H. Zhu, H. Ni, S. Liu, G. Xu, and L. Deng, "TNLRS: Target-aware non-local low-rank modeling with saliency filtering regularization for infrared small target detection," *IEEE Trans. Image Process.*, vol. 29, pp. 9546–9558, Oct. 2020.

[4] Q. Chen, M. Huang, H. Wang, and G. Xu, "A feature discretization method based on fuzzy rough sets for high-resolution remote sensing Big Data under linear spectral model," *IEEE Trans. Fuzzy Syst.*, vol. 30, no. 5, pp. 1328–1342, May 2021.

[5] D. Fu, H. Huang, X. Xiao, L. Xia, and L. Jin, "A generalized complex-valued constrained energy minimization scheme for the arctic sea ice extraction aided with neural algorithm," *IEEE Trans. Geosci. Remote Sens.*, vol. 60, Nov. 2021, Art. no. 4303017.

[6] Q. Chen, M. Huang, and H. Wang, "A feature discretization method for classification of high-resolution remote sensing images in coastal areas," *IEEE Trans. Geosci. Remote Sens.*, vol. 59, no. 10, pp. 8584–8598, Oct. 2021.

[7] C. Tian, L. Fei, W. Zheng, Y. Xu, W. Zuo, and C.-W. Lin, "Deep learning on image denoising: An overview," *Neural Netw.*, vol. 131, pp. 251–275, 2020.

[8] L. Zhuang, L. Gao, B. Zhang, X. Fu, and J. E. M. Bioucas-Dias, "Hyperspectral image denoising and anomaly detection based on low-rank and sparse representations," *IEEE Trans. Geosci. Remote Sens.*, vol. 60, Dec. 2022, Art. no. 5500117.

[9] Y. Wu, Y. Li, S. Feng, and M. Huang, "Pansharpening using unsupervised generative adversarial networks with recursive mixed-scale feature fusion," *IEEE J. Sel. Topics Appl. Earth Observ. Remote Sens.*, vol. 16, pp. 3742–3759, 2023.

[10] J.-S. Lee, "Digital image enhancement and noise filtering by use of local statistics," *IEEE Trans. Pattern Anal. Mach. Intell.*, vol. PAMI-2, no. 2, pp. 165–168, Mar. 1980.

[11] D. T. Kuan, A. A. Sawchuk, T. C. Strand, and P. Chavel, "Adaptive noise smoothing filter for images with signal-dependent noise," *IEEE Trans. Pattern Anal. Mach. Intell.*, vol. PAMI-7, no. 2, pp. 165–177, Mar. 1985.

[12] V. S. Frost, J. A. Stiles, K. S. Shanmugan, and J. C. Holtzman, "A model for radar images and its application to adaptive digital filtering of multiplicative noise," *IEEE Trans. Pattern Anal. Mach. Intell.*, vol. PAMI-4, no. 2, pp. 157–166, Mar. 1982.

[13] S. K. Maji, R. K. Thakur, and H. M. Yahia, "Structure-preserving denoising of SAR images using multifractal feature analysis," *IEEE Geosci. Remote Sens. Lett.*, vol. 17, no. 12, pp. 2100–2104, Dec. 2020.

[14] H. Aghababaei, G. Ferraioli, S. Vitale, R. Zamani, G. Schirinzi, and V. Pascazio, "Nonlocal model-free denoising algorithm for single-and multichannel SAR data," *IEEE Trans. Geosci. Remote Sens.*, vol. 60, Nov. 2022, Art. no. 5217315.

[15] J. Zhang, J. Chen, H. Yu, D. Yang, X. Xu, and M. Xing, "Learning an SAR image despeckling model via weighted sparse representation," *IEEE J. Sel. Topics Appl. Earth Observ. Remote Sens.*, vol. 14, pp. 7148–7158, Jul. 2021.

[16] R. Qin, X. Fu, J. Chang, and P. Lang, "Multilevel wavelet-SRNet for SAR target recognition," *IEEE Geosci. Remote Sens. Lett.*, vol. 19, Jan. 2022, Art. no. 4009005.

[17] D. Cozzolino, L. Verdoliva, G. Scarpa, and G. Poggi, "Nonlocal CNN SAR image despeckling," *Remote Sens.*, vol. 12, no. 6, 2020, Art. no. 1006.

[18] A. Sebastianelli, M. P. Del Rosso, S. L. Ullo, and P. Gamba, "A speckle filter for Sentinel-1 SAR ground range detected data based on residual convolutional neural networks," *IEEE J. Sel. Topics Appl. Earth Observ. Remote Sens.*, vol. 15, pp. 5086–5101, Jun. 2022.

[19] Z. Liu, R. Lai, and J. Guan, "Spatial and transform domain CNN for SAR image despeckling," *IEEE Geosci. Remote Sens. Lett.*, vol. 19, Sep. 2022, Art. no. 4002005.

[20] S. Liu, Y. Lei, L. Zhang, B. Li, W. Hu, and Y.-D. Zhang, "MRD-DANet: A multiscale residual dense dual attention network for SAR image denoising," *IEEE Trans. Geosci. Remote Sens.*, vol. 60, Sep. 2022, Art. no. 5214213.

[21] R. K. Thakur and S. K. Maji, "AGSDNet: Attention and gradient-based SAR denoising network," *IEEE Geosci. Remote Sens. Lett.*, vol. 19, Apr. 2022, Art. no. 4506805.

[22] E. Dalsasso, X. Yang, L. Denis, F. Tupin, and W. Yang, "SAR image despeckling by deep neural networks: From a pre-trained model to an end-to-end training strategy," *Remote Sens.*, vol. 12, no. 16, 2020, Art. no. 2636.

[23] W. Zhao, C.-A. Deledalle, L. Denis, H. Maître, J.-M. Nicolas, and F. Tupin, "Ratio-based multitemporal SAR images denoising: RABASAR," *IEEE Trans. Geosci. Remote Sens.*, vol. 57, no. 6, pp. 3552–3565, Jun. 2019.
[24] X. Ma, C. Wang, Z. Yin, and P. Wu, "SAR image despeckling by noisy reference-based deep learning method," *IEEE Trans. Geosci. Remote Sens.*, vol. 58, no. 12, pp. 8807–8818, Dec. 2020.
[25] T. Huang, S. Li, X. Jia, H. Lu, and J. Liu, "Neighbor2neighbor: Self-supervised denoising from single noisy images," in *Proc. IEEE/CVF Conf. Comput. Vis. Pattern Recognit.*, 2021, pp. 14781–14790.
[26] H. Lin, Y. Zhuang, Y. Huang, and X. Ding, "Self-supervised SAR despeckling powered by implicit deep denoiser prior," *IEEE Geosci. Remote Sens. Lett.*, vol. 19, Oct. 2022, Art. no. 4514705.
[27] S. Tan et al., "A CNN-based self-supervised synthetic aperture radar image denoising approach," *IEEE Trans. Geosci. Remote Sens.*, vol. 60, Aug. 2022, Art. no. 5213615.
[28] A. B. Molini, D. Valsesia, G. Fracastoro, and E. Magli, "Speckle2Void: Deep self-supervised SAR despeckling with blind-spot convolutional neural networks," *IEEE Trans. Geosci. Remote Sens.*, vol. 60, Aug. 2022, Art. no. 5204017.
[29] X. Feng, Q. Huang, and X. Li, "Ultrasound image de-speckling by a hybrid deep network with transferred filtering and structural prior," *Neurocomputing*, vol. 414, pp. 346–355, 2020.
[30] D. Ulyanov, A. Vedaldi, and V. Lempitsky, "Deep image prior," in *Proc. IEEE Conf. Comput. Vis. Pattern Recognit.*, 2018, pp. 9446–9454.
[31] W. Dong, P. Wang, W. Yin, G. Shi, F. Wu, and X. Lu, "Denoising prior driven deep neural network for image restoration," *IEEE Trans. Pattern Anal. Mach. Intell.*, vol. 41, no. 10, pp. 2305–2318, Oct. 2019.
[32] K. B. Eom, "Anisotropic adaptive filtering for speckle reduction in synthetic aperture radar images," *Opt. Eng.*, vol. 50, no. 5, 2011, Art. no. 057206.
[33] G. Aubert and J.-F. Aujol, "A variational approach to removing multiplicative noise," *SIAM J. Appl. Math.*, vol. 68, no. 4, pp. 925–946, 2008.
[34] K. Zhang, W. Zuo, Y. Chen, D. Meng, and L. Zhang, "Beyond a Gaussian denoiser: Residual learning of deep CNN for image denoising," *IEEE Trans. Image Process.*, vol. 26, no. 7, pp. 3142–3155, Jul. 2017.
[35] H. C. Burger, C. J. Schuler, and S. Harmeling, "Image denoising: Can plain neural networks compete with BM3D?," in *Proc. IEEE Conf. Comput. Vis. Pattern Recognit.*, 2012, pp. 2392–2399.
[36] T. Plotz and S. Roth, "Benchmarking denoising algorithms with real photographs," in *Proc. IEEE Conf. Comput. Vis. Pattern Recognit.*, 2017, pp. 1586–1595.
[37] K. Dabov, A. Foi, V. Katkovnik, and K. Egiazarian, "Image denoising by sparse 3-D transform-domain collaborative filtering," *IEEE Trans. Image Process.*, vol. 16, no. 8, pp. 2080–2095, Aug. 2007.
[38] K. Zhang, W. Zuo, S. Gu, and L. Zhang, "Learning deep CNN denoiser prior for image restoration," in *Proc. IEEE Conf. Comput. Vis. Pattern Recognit.*, 2017, pp. 3929–3938.
[39] K. Zhang, W. Zuo, and L. Zhang, "FFDNet: Toward a fast and flexible solution for CNN-based image denoising," *IEEE Trans. Image Process.*, vol. 27, no. 9, pp. 4608–4622, Sep. 2018.
[40] L. I. Rudin, S. Osher, and E. Fatemi, "Nonlinear total variation based noise removal algorithms," *Physica D*, vol. 60, no. 1/4, pp. 259–268, 1992.
[41] D. L. Donobo, "De-noising by soft-thresholding," *IEEE Trans. Inf. Theory*, vol. 41, no. 3, pp. 617–627, May 1995.
[42] G. Chierchia, D. Cozzolino, G. Poggi, and L. Verdoliva, "SAR image despeckling through convolutional neural networks," in *Proc. IEEE Int. Geosci. Remote Sens. Symp.*, 2017, pp. 5438–5441.
[43] K. He, X. Zhang, S. Ren, and J. Sun, "Deep residual learning for image recognition," in *Proc. IEEE Conf. Comput. Vis. Pattern Recognit.*, 2016, pp. 770–778.
[44] A. M. Teodoro, J. M. Bioucas-Dias, and M. A. Figueiredo, "Image restoration and reconstruction using variable splitting and class-adapted image priors," in *Proc. IEEE Int. Conf. Image Process.*, 2016, pp. 3518–3522.
[45] R. He, W.-S. Zheng, T. Tan, and Z. Sun, "Half-quadratic-based iterative minimization for robust sparse representation," *IEEE Trans. Pattern Anal. Mach. Intell.*, vol. 36, no. 2, pp. 261–275, Feb. 2014.
[46] O. Ronneberger, P. Fischer, and T. Brox, "U-Net: Convolutional networks for biomedical image segmentation," in *Proc. 18th Int. Conf. Med. Image Comput. Comput.-Assisted Intervention*, 2015, pp. 234–241.
[47] H. Zhao, O. Gallo, I. Frosio, and J. Kautz, "Loss functions for image restoration with neural networks," *IEEE Trans. Comput. Imag.*, vol. 3, no. 1, pp. 47–57, Mar. 2017.
[48] J. Canny, "A computational approach to edge detection," *IEEE Trans. Pattern Anal. Mach. Intell.*, vol. PAMI-8, no. 6, pp. 679–698, Nov. 1986.
[49] G. Sun, Q. Liu, Q. Liu, C. Ji, and X. Li, "A novel approach for edge detection based on the theory of universal gravity," *Pattern Recognit.*, vol. 40, no. 10, pp. 2766–2775, 2007.
[50] S. Q. Liu, S. H. Hu, Y. Xiao, and Y. L. An, "Bayesian Shearlet shrinkage for SAR image de-noising via sparse representation," *Multidimensional Syst. Signal Process.*, vol. 25, no. 4, pp. 683–701, 2014.
[51] C.-A. Deledalle, L. I. C. Denis, and F. Tupin, "Iterative weighted maximum likelihood denoising with probabilistic patch-based weights," *IEEE Trans. Image Process.*, vol. 18, no. 12, pp. 2661–2672, Dec. 2009.
[52] S. Liu et al., "Convolutional neural network and guided filtering for SAR image denoising," *Remote Sens.*, vol. 11, no. 6, 2019, Art. no. 702.
[53] S. Liu et al., "SAR speckle removal using hybrid frequency modulations," *IEEE Trans. Geosci. Remote Sens.*, vol. 59, no. 5, pp. 3956–3966, May 2020.
[54] R. K. Thakur and S. K. Maji, "SIFSDNet: Sharp image feature based SAR denoising network," in *Proc. IEEE Int. Geosci. Remote Sens. Symp.*, 2022, pp. 3428–3431.
[55] G. Cheng, J. Han, and X. Lu, "Remote sensing image scene classification: Benchmark and state of the art," *Proc. IEEE*, vol. 105, no. 10, pp. 1865–1883, Oct. 2017.
[56] A. Foi, V. Katkovnik, and K. Egiazarian, "PointWise shape-adaptive DCT for high-quality denoising and deblocking of grayscale and color images," *IEEE Trans. Image Process.*, vol. 16, no. 5, pp. 1395–1411, May 2007.
[57] R. Franzen, "Kodak lossless true color image suite," 1999. [Online]. Available: http://r0k.us/graphics/kodak
[58] L. Zhang, X. Wu, A. Buades, and X. Li, "Color demosaicking by local directional interpolation and nonlocal adaptive thresholding," *J. Electron. Imag.*, vol. 20, no. 2, 2011, Art. no. 023016.
[59] R. Zeyde, M. Elad, and M. Protter, "On single image scale-up using sparse-representations," in *Proc. 7th Int. Conf. Curves Surfaces*, 2012, pp. 711–730.
[60] Z. Wang, A. C. Bovik, H. R. Sheikh, and E. P. Simoncelli, "Image quality assessment: From error visibility to structural similarity," *IEEE Trans. Image Process.*, vol. 13, no. 4, pp. 600–612, Apr. 2004.
[61] S. G. Dellepiane and E. Angiati, "Quality assessment of despeckled SAR images," *IEEE J. Sel. Topics Appl. Earth Observ. Remote Sens.*, vol. 7, no. 2, pp. 691–707, Feb. 2014.
[62] H. Feng, B. Hou, and M. Gong, "SAR image despeckling based on local homogeneous-region segmentation by using pixel-relativity measurement," *IEEE Trans. Geosci. Remote Sens.*, vol. 49, no. 7, pp. 2724–2737, Jul. 2011.
[63] L. Gomez, R. Ospina, and A. C. Frery, "Unassisted quantitative evaluation of despeckling filters," *Remote Sens.*, vol. 9, no. 4, 2017, Art. no. 389.

Cong Lin received the B.S. degree in automation and the M.S. degree in control theory and control engineering from the Guangxi University of Science and Technology, Liuzhou, China, in 2011 and 2015, respectively. He is currently working toward the Ph.D. degree in information and communication engineering with Hainan University, Haikou, China.

He is also a Lecturer with the School of Information and Communication Engineering, Guangdong Ocean University, Zhanjiang, China. His current research interests include machine learning and image processing.

Chenghao Qiu received the B.S. degree in intelligent science and technology from Hainan University, Haikou, China, in 2023. He is currently working toward the M.S. degree in biomedical engineering with the University of Electronic Science and Technology of China, Chengdu, China.

His current research interests include computer vision tasks and biovisual information processing.

Haoyu Jiang received the bachelor's degree in energy and environmental systems engineering from the College of Energy Engineering, Zhejiang University, Hangzhou, China, in 2011, and the Ph.D. degree in engineering thermophysics from the State Key Laboratory of Clean Energy Utilization, Zhejiang University, in 2017.

He is currently an Associate Professor major in energy Internet with the School of Electronics and Information Engineering, Guangdong Ocean University, Zhanjiang, China, and the Director of Industrial Internet Company Ltd., Hangzhou. He has been with the Provincial Key Enterprise Research Institute of Cloud-Energy, Hangzhou Zhongheng Electric Company Ltd., since 2017, and a Postdoctoral Fellow with the School of Automation, Southeast University, Nanjing, China. His current research interests include optimization method of data quality characteristic curve prediction method state estimation and failure mode diagnosis.

Dr. Jiang is the Deputy Secretary-General of Cognitive System and Information Processing Committee, China Artificial Intelligence Society, and the committee member of the Chinese Society of Automation.

Lilan Zou received the M.S. degree in condensed matter physics from the Sun Yat-sen University, Guangzhou, China, in 2015. She is currently working toward the Ph.D. degree in materials science and engineering with Hainan University, Haikou, China.

She is also a Lecturer with the School of Information and Communication Engineering, Guangdong Ocean University, Zhanjiang, China. Her recent research interests focus on nonvolatile electronic devices, and their applications in neuromorphic computing and information processing.